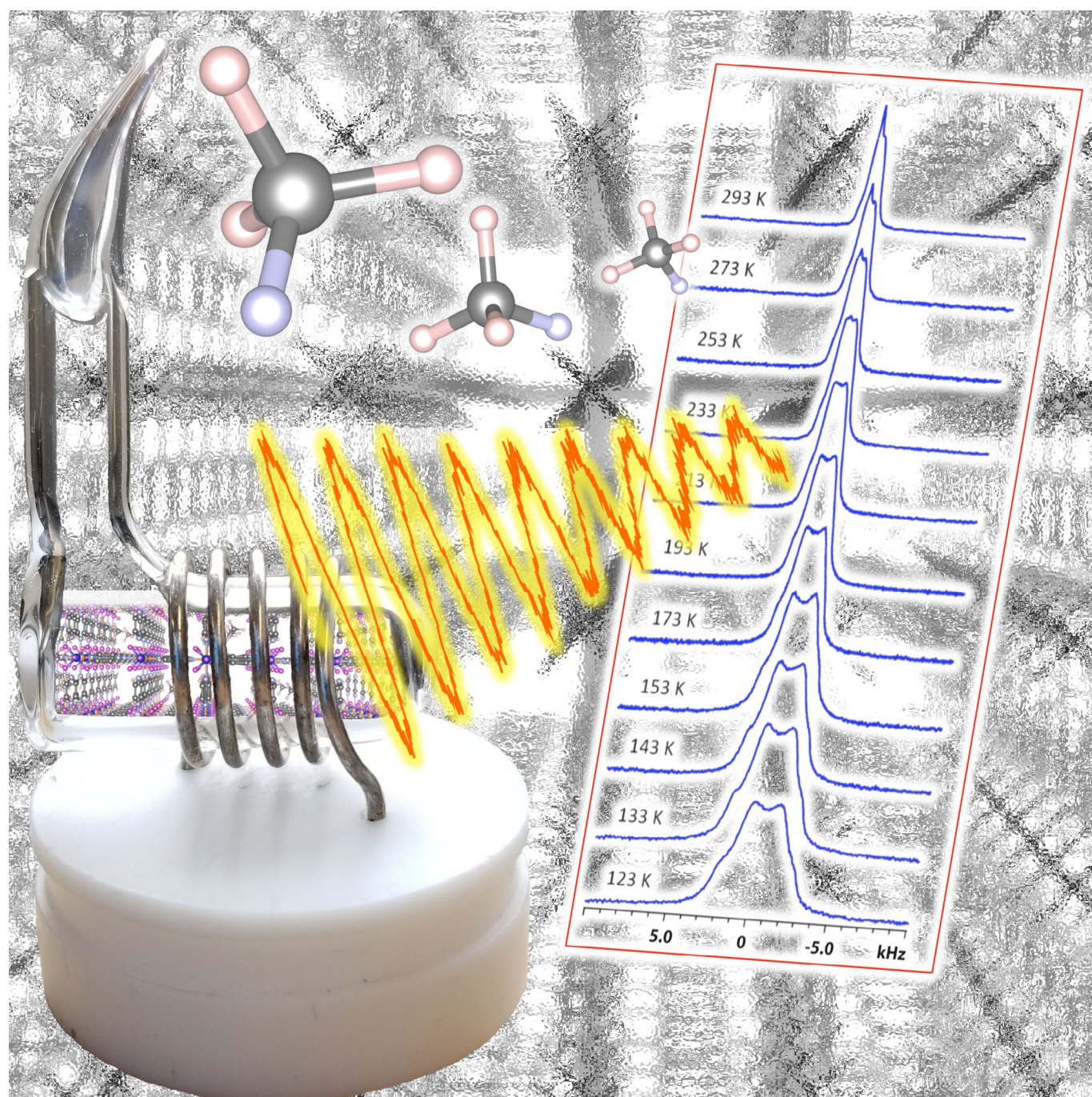


■ Metal–Organic Frameworks | *Very Important Paper* |

VIP A Multifaceted Study of Methane Adsorption in Metal–Organic Frameworks by Using Three Complementary Techniques

Yue Zhang,^[a] Bryan E. G. Lucier,^[a] Michael Fischer,^[b, c] Zhehong Gan,^[d] Paul D. Boyle,^[a] Bligh Desveaux,^[a] and Yining Huang^{*[a]}



Abstract: Methane is a promising clean and inexpensive energy alternative to traditional fossil fuels, however, its low volumetric energy density at ambient conditions has made devising viable, efficient methane storage systems very challenging. Metal–organic frameworks (MOFs) are promising candidates for methane storage. In order to improve the methane storage capacity of MOFs, a better understanding of the methane adsorption, mobility, and host–guest interactions within MOFs must be realized. In this study, methane adsorption within α -Mg₃(HCO₂)₆, α -Zn₃(HCO₂)₆, SIFSIX-3-Zn, and M-MOF-74 (M = Mg, Zn, Ni, Co) has been comprehensively examined. Single-crystal X-ray diffraction (SCXRD) experiments and DFT calculations of the methane adsorption locations were performed for α -Mg₃(HCO₂)₆, α -Zn₃(HCO₂)₆, and SIFSIX-3-Zn. The SCXRD thermal ellipsoids indicate that methane possesses significant mobility at the adsorption

sites in each system. ²H solid-state NMR (SSNMR) experiments targeting deuterated CH₃D guests in α -Mg₃(HCO₂)₆, α -Zn₃(HCO₂)₆, SIFSIX-3-Zn, and MOF-74 yield an interesting finding: the ²H SSNMR spectra of methane adsorbed in these MOFs are significantly influenced by the chemical shielding anisotropy in addition to the quadrupolar interaction. The chemical shielding anisotropy contribution is likely due mainly to the nuclear independent chemical shift effect on the MOF surfaces. In addition, the ²H SSNMR results and DFT calculations strongly indicate that the methane adsorption strength is linked to the MOF pore size and that dispersive forces are responsible for the methane adsorption in these systems. This work lays a very promising foundation for future studies of methane adsorption locations and dynamics within adsorbent MOF materials.

Introduction

With the rapid population growth and technological advances occurring in our modern world, the demand for energy is constantly increasing. The most commonly used energy sources are based on fossil fuels, which produce carbon dioxide emissions when combusted and are a main contributor to climate change phenomena including global warming. With this in mind, the development of alternative, cleaner energy sources is of great interest in order to stem the flow of CO₂ into the Earth's atmosphere.

Natural gas (NG), which mainly consists of methane, is an attractive substitute energy source due to its significant natural abundance, higher energy per unit mass versus all other hydrocarbons, and relatively lower carbon emissions as compared to typical fossil fuels.^[1] Despite the advantages of NG, its volu-

metric energy density at ambient temperature and pressure is much lower than that of gasoline, demanding the use of relatively large storage vessels and rendering CH₄ storage very challenging in applications where space is limited, such as automobiles.^[2] In addition, CH₄ gas is flammable and a safety hazard when stored in its pure form.

With the considerable storage and safety challenges associated with NG, attractive alternative strategies such as the adsorption and storage of CH₄ within porous and microporous materials have emerged in recent years.^[3] When using a porous adsorbent to store and release CH₄, the guest adsorption ability of the material is typically defined by the volumetric usable CH₄ capacity, which is the difference between the CH₄ capacity at the storage pressure (generally 35–65 bar) and the amount of CH₄ that remains within the adsorbent at the desorption pressure (generally 5.8 bar).^[1a,4] In this context, the development of adsorbents for NG storage with high volumetric usable CH₄ capacity is critical for implementing NG as a practical alternative energy source in many applications.

Metal–organic frameworks (MOFs) are a class of crystalline porous materials that are composed of metal ions or metal–inorganic clusters connected by organic bridging ligands.^[5] MOFs have many potential applications, including the adsorption and storage of various gases,^[6] such as methane.^[1a,7] By varying the topology and composition, the resulting MOF can be tailored to exhibit new or enhanced properties, including an increased methane adsorption capacity.^[6a] Many MOFs have exhibited promising CH₄ adsorption and storage capabilities.^[3b,7b] The highest documented usable CH₄ capacity (see above) in these materials is 150 and 190 v/v for adsorption at 35 and 65 bar, respectively, which was achieved by using a [Co(bdp)] (bdp = 1,4-benzenedipyrazolate) MOF as the adsorbent.^[8] Other MOFs, such as Basolite A520 (aluminum fumarate), have also shown promise as NG sorbents in automotive applications.^[9]

In order to move MOFs toward practical incorporation as CH₄ storage media and enhance the usable CH₄ capacity in

[a] Y. Zhang, B. E. G. Lucier, P. D. Boyle, B. Desveaux, Y. Huang
Department of Chemistry, The University of Western Ontario
1151 Richmond Street, London, Ontario, N6A 5B7 (Canada)
E-mail: yhuang@uwo.ca
Homepage: <http://publish.uwo.ca/~yhuang/index.htm>

[b] M. Fischer
Crystallography group, Department of Geosciences
University of Bremen, Klagenfurter Straße 2–4, D-28359 Bremen (Germany)

[c] M. Fischer
MAPEX Center for Materials and Processes, University of Bremen
D-28359 Bremen (Germany)

[d] Z. Gan
Centre of Interdisciplinary Magnetic Resonance
National High Magnetic Field Laboratory
1800 East Paul Dirac Drive, Tallahassee, FL, 32310 (USA)

 Supporting information (containing additional experimental details, detailed single-crystal XRD information, ²H SSNMR spectra and associated parameters of CH₃D, ²H SSNMR spectra of CD₄, powder XRD patterns, ORTEP illustrations of single-crystal XRD structures, and SCXRD details, along with three CIF files which correspond to CH₃D-saturated α -Zn₃(HCO₂)₆, CH₃D-saturated α -Mg₃(HCO₂)₆, and CH₃D-saturated SIFSIX-3-Zn and the ORCID identification numbers for the authors of this article can be found under: <https://doi.org/10.1002/chem.201800424>.

future MOFs, it is critical to obtain detailed knowledge of the host–guest interactions and the mobility of CH₄ within different kinds of MOFs. There are several experimental avenues for characterizing CH₄-loaded MOFs, investigating their CH₄ adsorption locations, and measuring the adsorption capacities. The most commonly employed method is to determine the CH₄ adsorption isotherms of the adsorbent MOF.^[10] The measured CH₄ adsorption isotherms provide useful information regarding the adsorption capacity and the isosteric heat of the CH₄ adsorption, but cannot locate the number and location of CH₄ adsorption sites within the MOF. Crystallographic and diffraction methods have been quite useful for investigating CH₄ adsorption in MOFs.^[11] In particular, neutron diffraction has been used to locate methane adsorption sites,^[12] however, obtaining detailed motional information is not possible. Single-crystal X-ray diffraction (SCXRD) is a very powerful and accessible characterization route for obtaining MOF and guest non-hydrogen atomic positions. Despite the wealth of structural information that can be obtained from in situ SCXRD studies of guest adsorption in MOFs, they remain uncommon,^[13] owing to the considerable difficulties in growing single crystals of many MOFs and locating relatively small and mobile species of low electron density (i.e., methane). Powder X-ray diffraction (pXRD) studies are useful in the many instances where growing MOF single crystals is very challenging or impossible, but extracting detailed structural information and/or crystal structures demands high-quality acquisitions and involves navigating a relatively complicated Rietveld refinement process. Nonetheless, pXRD has been used in several instances, such as for studying phase transitions in flexible MOFs during CH₄ adsorption.^[8,14] As a complementary tool, computational methods can be used to identify and refine methane adsorption locations in MOFs.^[15]

Solid-state NMR (SSNMR) spectroscopy is a sensitive probe of short-range structures^[16] and can provide detailed information on the guest adsorption, structure, mobility, and host–guest interactions in MOFs.^[13c,16c,d,f,17] NMR interactions are generally anisotropic and are affected by dynamics in a predictable manner, therefore, information regarding guest mobility and adsorption can be extracted from SSNMR spectra of gases within MOFs.^[18] ²H is an attractive target due to its nuclear properties. ²H has a nuclear spin of one and is subjected to the anisotropic quadrupolar interaction (QI) between the nuclear quadrupole moment and the surrounding electric field gradients (EFGs). Any motion that reorients the ²H EFG tensor influences the QI, and thus has an effect on the ²H SSNMR spectral line shape. Previous studies have proven that ²H SSNMR spectroscopy can provide rich information on the local structure, host–guest interactions, and dynamics of deuterated linkers^[19] and guests^[17e,f,20] such as D₂^[17e] in MOFs and microporous materials.

Herein, we describe a detailed SCXRD, computational, and SSNMR study of methane adsorption in four MOFs: α -Mg₃(HCO₂)₆ (HCO₂=formate), α -Zn₃(HCO₂)₆, SIFSIX-3-Zn, and M-MOF-74 (M=Mg, Zn, Ni, Co). This selection of MOFs allows for multiple comparisons, such as between MOFs which have the same topology but different metal centers (i.e., α -

Zn₂(HCO₂)₆ and α -Mg₂(HCO₂)₆), MOFs with very small channels (e.g., SIFSIX-3-Zn) versus those with relatively larger channels (e.g., MOF-74), and MOFs that have fully saturated metal centers (e.g., α -Mg₃(HCO₂)₆, α -Zn₃(HCO₂)₆, and SIFSIX-3-Zn) versus MOFs which have coordinatively unsaturated open metal sites (e.g., MOF-74). SCXRD has been used to accurately locate the methane adsorption sites. ²H SSNMR experiments were performed to probe the number of methane adsorption sites, understand host–guest interactions, and compare relative methane binding strengths within the MOFs. Plane-wave DFT calculations were also employed to confirm the number and location of adsorption sites within α -Mg₃(HCO₂)₆, α -Zn₃(HCO₂)₆, and SIFSIX-3-Zn as well as to calculate ²H NMR parameters. The knowledge gained in this work regarding adsorbed methane has clear practical implications for adapting and tailoring MOFs for the purposes of enhanced CH₄ adsorption and storage.

Experimental Section

MOF synthesis

All chemicals were obtained from Sigma–Aldrich and were used without further purification. The MOFs α -Mg₃(HCO₂)₆, α -Zn₃(HCO₂)₆, SIFSIX-3-Zn, Mg-MOF-74, Zn-MOF-74, Ni-MOF-74, and Co-MOF-74 were synthesized by using previously described methods^[21] with some slight modifications, and all details are included in the Supporting Information.

MOF activation

The sample activation procedure involves the use of heat and vacuum to purge residual solvent molecules from the pores of the as-made MOF. In order to prepare activated MOF samples, the as-made α -Mg₃(HCO₂)₆, α -Zn₃(HCO₂)₆, and SIFSIX-3-Zn samples were heated at 100, 150, and 80 °C, respectively, under dynamic vacuum (i.e., < 1 mbar) for at least twelve hours.

For Mg-MOF-74 only, an additional solvent-exchange step on the as-made sample was required before the activation process, which is briefly described here. A sample of the as-made Mg-MOF-74 (0.25 g) incorporating THF was solvent-exchanged by exposure to methanol (10 mL) in an autoclave at 200 °C for seven days. Each day, the autoclave was removed from the oven, brought to room temperature, and the methanol stock was replaced. After seven days, the THF was fully replaced by methanol within Mg-MOF-74. In the final step, the methanol-exchanged Mg-MOF-74 sample was heated at 250 °C under dynamic vacuum for eight hours, thereby purging all methanol and generating the activated Mg-MOF-74 sample.

Gas adsorption and loading within the MOFs

A Schlenk line was used for all gas adsorption and loading procedures. The MOF sample was first loaded into the bottom of a homemade 5 mm L-shaped glass tube. A thin layer of glass wool was then inserted above the sample in the tube in order to secure the sample in place. The glass tube was then attached to the Schlenk line and sample activation was performed. After activation, a known amount of pressurized CH₃D was introduced to the vacuum line and the CH₃D gas was allowed to occupy both the vacuum line and the glass tube containing the sample, which has a measured volume of approximately 82.7 cm³. The bottom of the CH₃D-filled glass tube was then immersed in liquid nitrogen to

freeze the CH₃D within the sample, and the glass tube end (now containing both CH₃D and the MOF sample) was then flame-sealed off from the Schlenk line. The overall CH₃D loading amount is expressed by the molar ratio between CH₃D and the metal. For the ²H SSNMR experiments in this study, 0.1 CH₃D per metal samples were prepared for the MOFs α-Mg₃(HCO₂)₆ and α-Zn₃(HCO₂)₆, whereas 0.2 CH₃D per metal samples were prepared for the MOFs SIFSIX-3-Zn and Mg-MOF-74.

Powder X-ray diffraction

The identity of all MOF products was confirmed through the use of powder XRD experiments, which were performed on an Inel CPS powder diffractometer operating with Cu_{Kα} radiation (λ = 1.5406 Å). Reflections were collected at 2θ values ranging from 5 to 120° with a total acquisition time of approximately three minutes for each pXRD pattern. All pXRD patterns are illustrated in Figure S1 in the Supporting Information.

Single-crystal X-ray diffraction (SCXRD)

The CH₃D-loaded MOF single-crystal samples were prepared by using a Schlenk line and the same gas adsorption procedure described above for the SSNMR samples, however, the gas loading level for the SCXRD samples was set to saturation rather than a defined loading ratio or amount. After gas loading and flame sealing, the glass tubes were broken, and the methane-saturated samples were immediately coated with paratone oil in order to retain as much methane gas as possible within the MOFs. An optical microscope was then used to select high-quality single crystals for the structural analysis.

All SCXRD measurements were performed on a Bruker Kappa Axis Apex2 diffractometer at a temperature of 110 K. The frame integration was performed by using SAINT.^[22] The resulting raw data were scaled and absorption corrected by using a multi-scan averaging of symmetry equivalent data with SADABS.^[23] The methane-loaded MOF structures were solved by using a dual space methodology incorporated in the SHELXT program.^[24] All non-hydrogen framework atoms were obtained from the initial structural solution. The hydrogen atoms were then introduced at idealized positions and were allowed to ride on the parent atom. The carbon atomic positions for the methane molecules were obtained from a difference Fourier map. The structural model was fit to the data by using a full-matrix least-squares method based on F². The calculated structure factors included corrections for anomalous dispersion from the usual tabulation. The structure was refined by using the SHELXL-2014 program from the SHELX suite of crystallographic software.^[25] Graphic plots were produced by using the NRCVAX program suite.^[26] A detailed summary of the crystallographic data of methane-loaded α-Mg₃(HCO₂)₆, α-Zn₃(HCO₂)₆, and SIFSIX-3-Zn are given in appendix A of the Supporting Information.

Density-functional theory calculations

DFT calculations for the methane-loaded MOFs were performed by using the CASTEP code.^[27] The calculations used the PBE exchange-correlation functional^[28] in conjunction with the D2 dispersion correction devised by Grimme.^[29] All NMR parameters were calculated employing the gauge-including projector-augmented waves (GIPAW) formalism.^[30] Further details on the calculations are included in the Supporting Information.

²H solid-state NMR experiments

All SSNMR experiments were performed on a wide-bore Varian/Chemagnetics InfinityPlus NMR spectrometer operating at 9.4 T (ν₀(²H) = 61.32 MHz) with a 5 mm static HX probe. A sample of D₂O (l) was used as a secondary chemical shift reference at δ_{iso} = 4.8 ppm with respect to neat (CD₃)₄Si.^[31] The experimental temperature was controlled by a Varian VT control unit, and all temperatures were calibrated to ± 3 K by using the ²⁰⁷Pb chemical shift of a solid sample of lead nitrate across the experimental temperature range.^[32] A quadrupolar echo pulse sequence of the format (π/2-τ₁-π/2-τ₂) was used to acquire the ²H NMR spectra, employing a π/2 pulse width of 4.5 μs, an interpulse τ₁ time of 45 μs, and a τ₂ duration of 25 μs. A ¹H-decoupling field of approximately 63 kHz was applied during all ²H SSNMR experiments. All spectra were acquired by using calibrated ²H pulse delays ranging from 1 to 3 s, depending on the sample and experimental temperature. A spectral width of 20 kHz was employed for ²H SSNMR experiments involving CH₃D and CH₂D₂ adsorbed in α-Mg₃(HCO₂)₆, α-Zn₃(HCO₂)₆, and Mg-MOF-74; however, a spectral width of 30 kHz was required for ²H SSNMR experiments on CH₃D and CH₂D₂ adsorbed within SIFSIX-3-Zn.

Spectral simulation software

The WSolidS^[33] computer software was used to perform analytical simulations of the experimental SSNMR spectra in order to obtain the apparent or observed ²H NMR parameters.

Results and Discussion

Methane adsorption within α-Mg₃(HCO₂)₆

MOFs with small pores tend to have stronger interactions with some guests.^[1a,7] α-Mg₃(HCO₂)₆ is an ultra-microporous MOF with relatively small one-dimensional zigzag-shaped channels that measure approximately 4.8 Å in diameter.^[21a] CH₄ adsorption studies^[34] and DFT calculations^[35] have indicated that α-Mg₃(HCO₂)₆ is a promising methane adsorbent and possesses a good selectivity of CH₄ over N₂ gas.^[34b,35] However, there has not been a comprehensive investigation of α-Mg₃(HCO₂)₆ to determine the specific methane adsorption site locations and host-guest interactions involved. We have performed an intertwined SCXRD, computational, and SSNMR investigation of methane adsorption within α-Mg₃(HCO₂)₆.

SCXRD and DFT investigations of methane-loaded α-Mg₃(HCO₂)₆

In this study, SCXRD has been used to unambiguously determine the number and location of methane adsorption sites in α-Mg₃(HCO₂)₆. For ease of comparison with ²H SSNMR experiments, singly deuterated CH₃D guests were used rather than CH₄; see the ²H SSNMR section for more details. The carbon atomic positions of the CH₃D guests within α-Mg₃(HCO₂)₆ have been successfully obtained from SCXRD experiments at 110 K. The methane carbon positions established from SCXRD are shown from two different perspectives in Figure 1 a and b. Although a MOF sample saturated with CH₃D was used, the SCXRD results indicate that the CH₃D occupancy is actually 0.25 (i.e., 1.0 CH₃D per unit cell) under these experimental con-

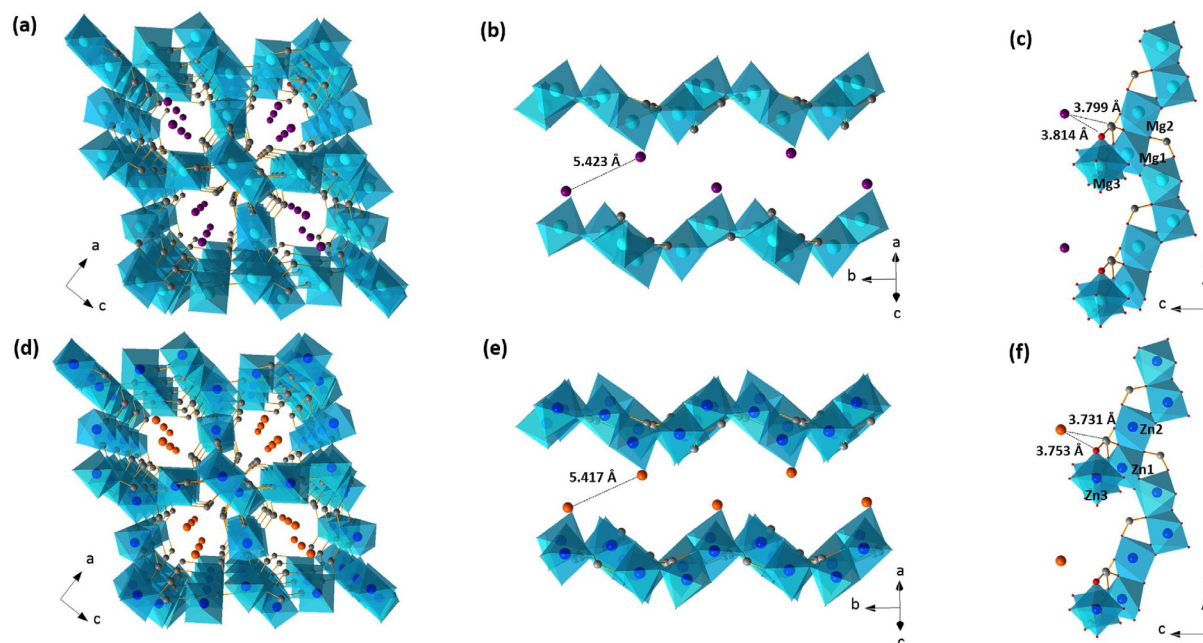


Figure 1. a) Extended framework structure of the CH₃D-loaded MOF α -Mg₃(HCO₂)₆, as viewed along the crystallographic *b* axis. b) Locations of the CH₃D carbon atoms (colored purple) along one of the zigzag-shaped channels of α -Mg₃(HCO₂)₆. c) Shortest distances between the adsorbed CH₃D carbon atom and the framework atoms of α -Mg₃(HCO₂)₆. d) Extended long-range structure of the CH₃D-loaded MOF α -Zn₃(HCO₂)₆, as viewed along the crystallographic *b* axis. e) Local positions of adsorbed CH₃D carbon atoms (colored orange) within its zigzag-shaped channels. f) Shortest distances between the carbon atom of CH₃D and the atoms of the α -Zn₃(HCO₂)₆ framework. Carbon is colored gray, oxygen is red, zinc is blue, magnesium is light blue, purple denotes the carbon atoms of CH₃D within α -Mg₃(HCO₂)₆, and orange spheres represent carbon atoms of CH₃D molecules within α -Zn₃(HCO₂)₆. Detailed information on the DFT-optimized methane-loaded α -Mg₃(HCO₂)₆ and α -Zn₃(HCO₂)₆ structures can be found in Figure 2 and Figure S8 in the Supporting Information, respectively.

ditions, which is likely due to a loss of CH₃D when transferring the guest-loaded single crystal to the diffractometer.

There are two symmetry-equivalent methane adsorption sites in each channel, and two symmetry-equivalent channels are present in each unit cell, yielding four equivalent methane adsorption sites but only one crystallographically unique methane site per unit cell. The two symmetry-related methane adsorption sites in each channel are located 5.423 Å apart, on the opposite sides of the zigzag-shaped MOF channels that run along the crystallographic *b* axis (Figure 1b). The CH₃D carbon atom lies 3.799 Å away from the carbon atom of the formate linker and 3.814 Å away from the oxygen atom on the same formate linker (Figure 1c). The position of the CH₃D carbon atom suggests that the hydrogen and oxygen atoms of the formate linker play a role in the methane adsorption within α -Mg₃(HCO₂)₆ through weak and distant interactions. The thermal ellipsoid of the methane carbon atom was also obtained from SCXRD measurements (Figures S2 and S3a in the Supporting Information) and is relatively large, particularly along the direction of the zigzag-shaped channels in α -Mg₃(HCO₂)₆ and toward the adjacent symmetry-equivalent methane carbon atom, implying that methane rapidly moves between adjacent adsorption sites located along the channels.

In order to further understand the methane adsorption in α -Mg₃(HCO₂)₆, we have performed a detailed DFT study involving 1) optimization of the methane location, 2) calculation of the adsorption site energy, and 3) calculations of the ²H NMR parameters (see below). The guest methane molecule location was optimized along with the positions of all atoms in the

MOF (see appendix A in the Supporting Information). The results of the DFT geometry optimizations are shown from a short-range (Figure S4 in the Supporting Information) and a long-range (Figure 2) perspective. In the DFT-optimized structure, the methane adsorption site is quite proximate to the SCXRD methane carbon position and lies well inside the carbon displacement ellipsoid (Figure 2). The geometry-optimized structure (Figure 2) shows that the closest distance between the hydrogen atom of a static methane molecule and a framework oxygen atom is 2.780 Å, confirming that the oxygen atom of the linker plays a role in the methane adsorption.

The specific methane adsorption energy at the DFT-optimized methane location within α -Mg₃(HCO₂)₆ at the SCXRD methane loading level of 1.0 molecules per unit cell was determined to be -25.1 kJ mol⁻¹. The dispersive contribution was calculated as -20.3 kJ mol⁻¹ (Table S1 in the Supporting Information), implying that van der Waals forces drive the methane adsorption in this system, whereas electrostatics play a minor role. The methane adsorption energy is not strongly influenced by the methane loading level; the calculated value only changes very slightly to -25.7 kJ mol⁻¹ when the loading level is quadrupled to 4.0 methane molecules per unit cell. It should be noted that the large methane carbon displacement ellipsoid from SCXRD suggests that there is a large region near the methane adsorption site where the adsorption energies are quite similar.

To verify the presence of a single unique methane adsorption site, and to probe the local environment and dynamics of

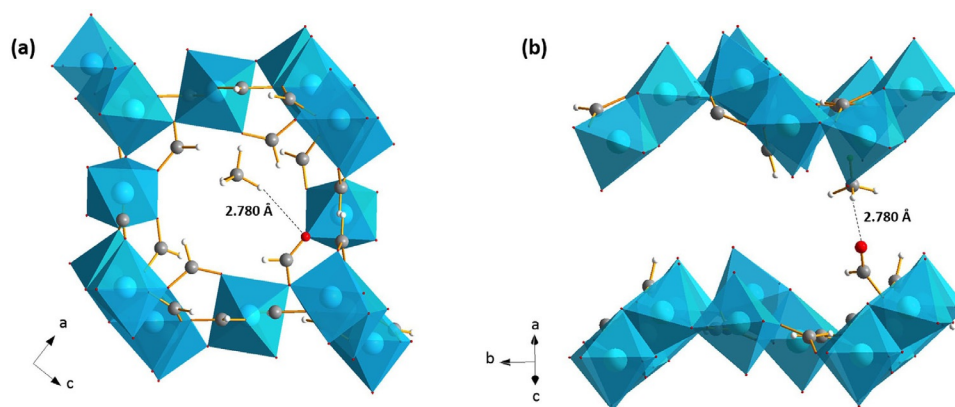


Figure 2. The DFT-optimized methane-loaded α - $\text{Mg}_3(\text{HCO}_2)_6$ structure at a loading level of 1.0 methane per unit cell is shown from various perspectives. The shortest distances between the DFT-optimized adsorbed methane hydrogen atoms and the framework atoms of α - $\text{Mg}_3(\text{HCO}_2)_6$ are depicted in a) and b) from two different projections. The colors blue, gray, and white correspond to the magnesium metal center, carbon, and hydrogen, respectively. The methane hydrogen atoms were added computationally and their positions were also optimized.

adsorbed methane guests, ^2H SSNMR experiments were performed.

Investigating methane within α - $\text{Mg}_3(\text{HCO}_2)_6$ through ^2H SSNMR spectroscopy

Static variable-temperature (VT) ^2H SSNMR experiments on singly deuterated methane (CH_3D) adsorbed in α - $\text{Mg}_3(\text{HCO}_2)_6$ were performed at temperatures ranging from 123 to 293 K. The experimental static VT ^2H SSNMR spectra of CH_3D adsorbed within α - $\text{Mg}_3(\text{HCO}_2)_6$ at a loading level of 0.1 CH_3D per Mg (1.2 CH_3D molecules per unit cell) are shown in Figure 3a. At 293 K, a sharp resonance is present, which corresponds to

rapidly and isotropically tumbling CH_3D . The anisotropic quadrupolar interaction is typically the primary origin of ^2H spectral broadening and dominates the ^2H SSNMR spectral appearance; when CH_3D is rapidly isotropically tumbling, the ^2H EFG tensor is reoriented through all possible directions, removing the anisotropy of the QI and eliminating the broadening effects of the QI on the ^2H SSNMR spectrum. It should be noted that the chemical shift (CS) interaction may also influence and broaden the ^2H SSNMR spectra; however, much like the case of the QI, rapid isotropic tumbling removes the CS anisotropy (CSA) and eliminates its spectral effects.

As the temperature is reduced, the ^2H spectra of CH_3D adsorbed within α - $\text{Mg}_3(\text{HCO}_2)_6$ gradually grow broader. Experi-

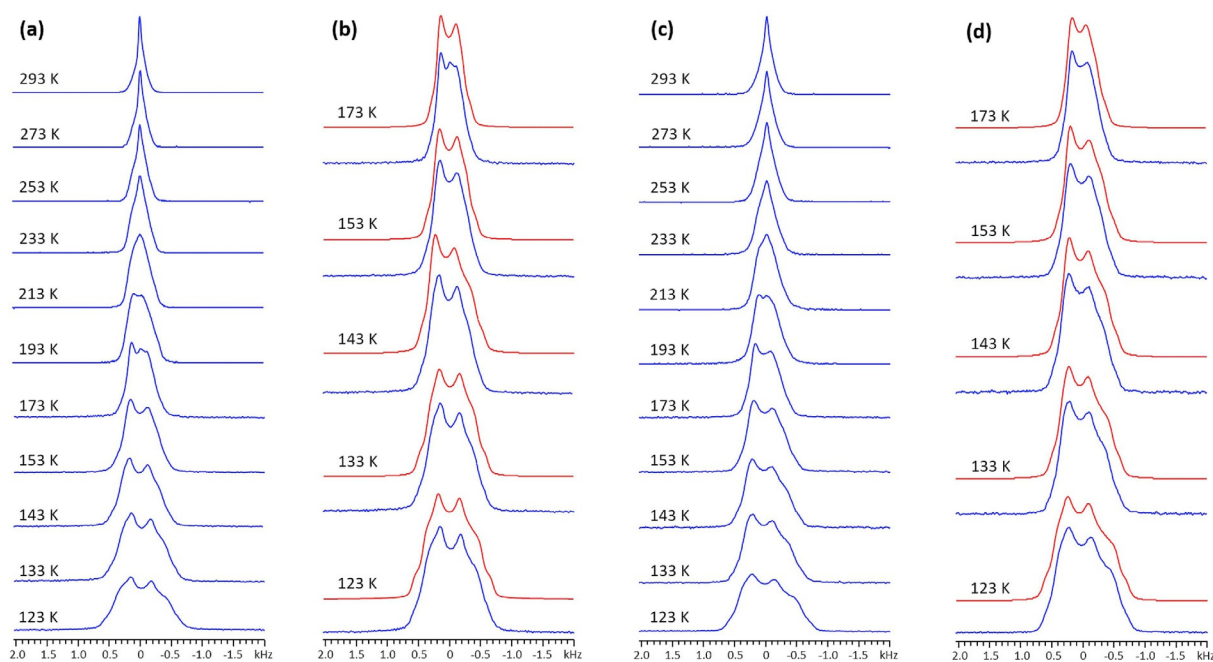


Figure 3. a) Experimental static VT ^2H SSNMR spectra of CH_3D adsorbed within α - $\text{Mg}_3(\text{HCO}_2)_6$. b) Comparison of the experimental (blue) and analytical simulated (red) low-temperature ^2H SSNMR spectra. c) Experimental static VT ^2H SSNMR spectra of CH_3D adsorbed within α - $\text{Zn}_3(\text{HCO}_2)_6$. d) Comparison of the experimental (blue) and analytical simulated (red) ^2H SSNMR spectra of CH_3D in α - $\text{Zn}_3(\text{HCO}_2)_6$ at low temperatures.

mental ^2H powder patterns at and below 173 K exhibit characteristic features and line shapes that can be simulated to extract the apparent NMR parameters. Each ^2H SSNMR spectrum between 173 and 123 K features one ^2H powder pattern, which indicates that adsorbed CH_3D resides at a single crystallographically unique adsorption site within $\alpha\text{-Mg}_3(\text{HCO}_2)_6$ at this loading level. The observation of a single powder pattern is in excellent agreement with the one crystallographically unique methane molecule adsorption site evident from the SCXRD experiments. The observed $C_Q(^2\text{H})$ values of CH_3D adsorbed within $\alpha\text{-Mg}_3(\text{HCO}_2)_6$ increase from 460 Hz at 173 K to 860 Hz at 123 K, whereas the η_Q values also rise from 0.23 at 173 K to 0.47 at 123 K (Table 1). It is particularly noteworthy that the observed $C_Q(^2\text{H})$ values are less than 0.5% the magnitude of the reported^[36] and DFT-calculated $C_Q(^2\text{H})$ values (Table S2 in the Supporting Information) of a single static CH_3D molecule, which are both 192 kHz. The vastly smaller observed experimental $C_Q(^2\text{H})$ values and diminished apparent QI are a clear sign that we are observing a time-averaged ^2H SSNMR spectrum involving fast exchange between CH_3D isotropically tumbling in the pores and CH_3D undergoing anisotropic motion. It should be noted that these ^2H line shapes could not be motionally simulated^[18] by using motional rates in the slow ($1\text{--}10^3\text{ s}^{-1}$) or intermediate ($10^3\text{--}10^6\text{ s}^{-1}$) ranges, only the fast motional regime ($>10^7\text{ s}^{-1}$).

Curiously, the ^2H powder patterns exhibit distorted line shapes that significantly stray from that of a typical QI-domi-

nated ^2H Pake doublet.^[37] The only method to simulate this peculiar ^2H line shape is by introducing the effects of CSA, which has been known to contribute to the ^2H NMR line shapes in select instances.^[38] The observed ^2H span value of 0.8 ppm is smaller than the plane-wave DFT-calculated span value of 9.0 ppm (Table S2 in the Supporting Information), which can be attributed to the nearly isotropic tumbling of CH_3D that diminishes the CSA and reduces the apparent span to a significantly smaller value. The ^2H CS and QI of CH_3D are subject to very different magnitudes of time-averaged motional scaling in this MOF: the observed span values are approximately 9% of the calculated span value, whereas the observed $C_Q(^2\text{H})$ values are less than 0.5% of the calculated and reported $C_Q(^2\text{H})$ values.

The additional CS contribution has two likely origins: anisotropic bulk magnetic susceptibility (ABMS) and nucleus-independent chemical shift (NICS). The effects of ABMS broadening have been observed in many systems,^[39] including MOFs.^[40] ABMS broadening in a sample can readily be identified, for example, by a characteristic anisotropic inclination or "tilting" of cross peaks in 2D $^1\text{H}\rightarrow^{13}\text{C}$ HETCOR spectra. A review of the previous 2D $^1\text{H}\rightarrow^{13}\text{C}$ HETCOR experiments on various forms of $\alpha\text{-Mg}_3(\text{HCO}_2)_6$ shows that the cross peaks are largely linear with minimal "tilting."^[41] In the case of aromatic guests, the very slight observed tilting of cross peaks is far less severe than in typical HETCOR spectra of compounds known to exhibit strong ABMS.^[39,40] To confirm that ABMS is indeed not a major contributor to ^2H CSA in this system, ^2H SSNMR experiments were performed on samples of methane-loaded $\alpha\text{-Mg}_3(\text{HCO}_2)_6$ significantly diluted in KBr, which has an isotropic magnetic susceptibility; the ^2H CSA effects persist in these samples (Figure S5 in the Supporting Information), indicating that ABMS has little (or a very minor) contribution. Thus, the likely culprit for the different magnitudes of EFG and CS motional averaging appears to be the NICS,^[42] which is now discussed.

In this system, the NICS refers to a specific phenomenon where the presence of an external magnetic field influences the electrons of the MOF to circulate and produce an induced magnetic field within the MOF, particularly near the MOF surfaces. As guest methane molecules become adsorbed to the MOF, the induced magnetic field generated by the electrons of the MOF influences the local magnetic environment around the ^2H nuclei within the methane guests, thereby increasing the apparent ^2H CSA and also making a contribution to the ^2H isotropic chemical shift (Table 1). Previous studies have indicated that the magnitude of the NICS is closely linked to the adsorbent-adsorbate distance,^[43] or in this case, the MOF-methane distance. As guest methane molecules approach the MOF surface and become adsorbed, the magnitudes of the NICSs increase, resulting in more significant contributions to the ^2H CSA and isotropic chemical shift (Figure 4). It should be noted that many observations of the NICS have been in porous carbons and graphite, owing to the ring-current effects that occur in their fused sp^2 -hybridized networks. In MOFs such as $\alpha\text{-Mg}_3(\text{HCO}_2)_6$, there is no such fused sp^2 network, however, all the MOF surface elements are ordered (i.e., aligned and orient-

Table 1. Observed ^2H NMR parameters of CH_3D adsorbed in four different MOFs, as obtained at different experimental temperatures.

| MOF | T [K] | C_Q [Hz] | η_Q | Ω [ppm] | κ | δ_{iso} [ppm] | β^{al} [°] |
|--------------------------------------|-------|------------|----------|----------------|----------|-----------------------------|-------------------------|
| $\alpha\text{-Mg}_3(\text{HCO}_2)_6$ | 123 | 860(10) | 0.47(3) | 0.8(5) | -1.0(5) | -0.7(1) | 0(30) |
| | 133 | 760(10) | 0.42(3) | 0.8(5) | -1.0(5) | -0.6(1) | 0(30) |
| | 143 | 660(10) | 0.38(2) | 0.8(5) | -1.0(5) | -0.5(1) | 0(30) |
| | 153 | 570(10) | 0.33(2) | 0.8(5) | -1.0(5) | -0.4(1) | 0(30) |
| | 173 | 460(10) | 0.23(2) | 0.8(5) | -1.0(5) | -0.3(1) | 0(30) |
| $\alpha\text{-Zn}_3(\text{HCO}_2)_6$ | 123 | 920(10) | 0.50(3) | 2.0(5) | -1.0(5) | -0.4(1) | 0(30) |
| | 133 | 770(10) | 0.45(3) | 2.0(5) | -1.0(5) | -0.4(1) | 0(30) |
| | 143 | 710(10) | 0.40(3) | 2.0(5) | -1.0(5) | -0.3(1) | 0(30) |
| | 153 | 640(10) | 0.30(2) | 2.0(5) | -1.0(5) | -0.2(1) | 0(30) |
| | 173 | 500(10) | 0.20(2) | 2.0(5) | -1.0(5) | -0.2(1) | 0(30) |
| SIFSIX-3-Zn | 123 | 3700(80) | 0.35(3) | 2.5(5) | -1.0(5) | -2.0(2) | 80(10) |
| | 133 | 3400(80) | 0.33(3) | 2.5(5) | -1.0(5) | -2.0(2) | 80(10) |
| | 143 | 3000(50) | 0.31(3) | 2.5(5) | -1.0(5) | -2.0(2) | 80(10) |
| | 153 | 2700(50) | 0.30(3) | 2.5(5) | -1.0(5) | -2.0(2) | 80(10) |
| | 173 | 2200(20) | 0.30(3) | 2.5(5) | -1.0(5) | -2.0(2) | 80(10) |
| | 193 | 1800(20) | 0.27(3) | 2.5(5) | -1.0(5) | -2.0(2) | 80(10) |
| | 213 | 1520(20) | 0.25(3) | 2.5(5) | -1.0(5) | -2.0(2) | 80(10) |
| Mg-MOF-74 | 123 | 620(5) | 0.00(5) | 2.0(5) | -1.0(5) | -0.8(1) | 80(10) |
| | 128 | 570(5) | 0.00(5) | 2.0(5) | -1.0(5) | -0.8(1) | 80(10) |
| | 133 | 520(5) | 0.00(5) | 2.0(5) | -1.0(5) | -0.8(1) | 80(10) |
| | 138 | 480(5) | 0.00(5) | 2.0(5) | -1.0(5) | -0.8(1) | 80(10) |
| | 143 | 420(5) | 0.00(5) | 2.0(5) | -1.0(5) | -0.8(1) | 80(10) |

[a] The angle β refers to the Euler angle between the V_{33} component of the EFG tensor and the δ_{33} component of the CS tensor. The other Euler angles were not found to significantly impact spectral appearance.

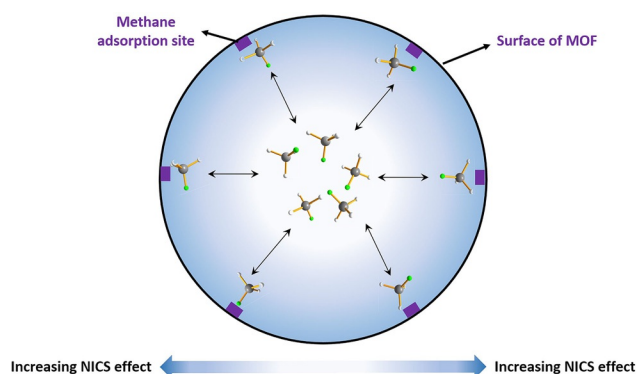


Figure 4. Simplified illustration of the NICS effect on methane guests in a MOF. As CH_3D molecules approach the MOF surface, the magnitudes of the NICSs increase, resulting in more significant contributions to the ^2H CSA and isotropic chemical shift.

ed in the same direction) regardless of hybridization. This ordering avoids any cancellation of the induced magnetic field near the MOF surface, so the respective chemical shift contributions from all surface elements to the shift are added together.

In $\alpha\text{-Mg}_3(\text{HCO}_2)_6$, CH_3D molecules undergoing isotropic tumbling in the MOF pores are in fast exchange with adsorbed CH_3D guests proximate to the MOF surface that are undergoing anisotropic motion; the ^2H SSNMR spectra of CH_3D reflect a time-averaged picture of both CH_3D methane species. The time-averaged motional scaling factor of the QI and CSA determines the ^2H NMR line width and line shape. The motional scaling factor is the same for the QI and CSA; however, the NICS effect introduces additional CSA in adsorbed methane molecules located near the MOF surface. As the temperature is lowered, more methane guests are adsorbed, and methane spends a relatively longer time at the MOF surfaces. The time-averaged population of adsorbed versus free methane guests is altered, which in turn influences the time-averaged motional scaling factor of the CSA, because more methane molecules are now adsorbed and subject to the NICS effect. The net effect on the ^2H SSNMR spectra of methane is a larger apparent CSA due to the NICS contribution. This is especially significant because, to the best of our knowledge, NICS effects have not yet been reported for guest molecules in MOFs. In addition, the ^2H δ_{iso} values decrease for methane adsorbed within $\alpha\text{-Mg}_3(\text{HCO}_2)_6$ as the temperature is reduced (Table 1), reflecting increased contributions from the NICS as the time-averaged methane populations evolve.

The DFT calculation results are also consistent with the NICS presence in $\alpha\text{-Mg}_3(\text{HCO}_2)_6$. Methane was placed at five distinct locations in the MOF pores, a geometry optimization was performed, and then the ^2H NMR parameters for methane deuterium were calculated. The five locations included the geometry-optimized SCXRD adsorption site and an alternate location within the SCXRD thermal ellipsoid. Methane was also placed in three additional positions located outside of the thermal ellipsoid (Figure S6 in the Supporting Information) with different distances to the wall of the framework. A clear correlation is evident between the calculated ^2H span values and the dis-

tance from the methane deuterium atom to the nearest framework atom (Table S3 in the Supporting Information); as the methane molecule draws closer to the pore wall, the DFT calculations indicate that the ^2H span value increases, reflecting an increased NICS contribution to ^2H CSA and supporting our experimental VT ^2H NMR findings. Unfortunately, no clear trend in the calculated ^2H isotropic chemical shielding values was evident as the methane position was varied, indicating that a more detailed future computational study is likely required to fully examine the NICS phenomenon in $\alpha\text{-Mg}_3(\text{HCO}_2)_6$.

Methane adsorption within $\alpha\text{-Zn}_3(\text{HCO}_2)_6$

The MOF $\alpha\text{-Zn}_3(\text{HCO}_2)_6$ is analogous to $\alpha\text{-Mg}_3(\text{HCO}_2)_6$, featuring zinc metal centers and formate linkers that form a similar 3D crystalline structure,^[21b] with a slightly smaller channel diameter of 4.44 Å in the Zn analogue versus 4.58 Å in the Mg variant.^[35] Although CH_4 adsorption in $\alpha\text{-Zn}_3(\text{HCO}_2)_6$ has not been extensively studied, a recent computational study has indicated that $\alpha\text{-Zn}_3(\text{HCO}_2)_6$ exhibits a stronger interaction with methane than $\alpha\text{-Mg}_3(\text{HCO}_2)_6$; the reported calculated adsorption energy of methane within $\alpha\text{-Zn}_3(\text{HCO}_2)_6$ is -27.6 versus -25.7 kJ mol^{-1} in $\alpha\text{-Mg}_3(\text{HCO}_2)_6$.^[35] In order to establish the methane adsorption site locations in $\alpha\text{-Zn}_3(\text{HCO}_2)_6$ and to understand the reasons for the subtle difference in the methane adsorption energies between the two formate MOFs, SCXRD, DFT, and ^2H SSNMR experiments have been performed on $\alpha\text{-Zn}_3(\text{HCO}_2)_6$.

SCXRD and DFT calculations of methane-loaded $\alpha\text{-Zn}_3(\text{HCO}_2)_6$

The CH_3D adsorption sites within $\alpha\text{-Zn}_3(\text{HCO}_2)_6$ have been successfully located by using SCXRD. The occupancy of CH_3D within CH_3D -saturated $\alpha\text{-Zn}_3(\text{HCO}_2)_6$ at our experimental loading level was determined to be 0.33 (1.32 molecules per unit cell), which is slightly higher than that of $\alpha\text{-Mg}_3(\text{HCO}_2)_6$ (1.0 molecule per unit cell). The CH_3D adsorption sites in the crystal structure of CH_3D -saturated $\alpha\text{-Zn}_3(\text{HCO}_2)_6$ are shown in Figure 1 d, and are located in a similar position as those within $\alpha\text{-Mg}_3(\text{HCO}_2)_6$. There are two symmetry-equivalent CH_3D adsorption sites. The two symmetry-equivalent methane adsorption sites are located 5.417 Å apart and can be found on opposite sides of the zigzag-shaped channels that run along the crystallographic *b* axis (Figure 1 e). The ORTEP drawing of the $\alpha\text{-Zn}_3(\text{HCO}_2)_6$ structure about the methane adsorption site (Figure S7 in the Supporting Information) highlights the relatively large thermal ellipsoid associated with the methane carbon atom. The large thermal ellipsoid indicates that despite the observation of a single unique methane adsorption site in this system, there is a rather large area of similar interaction strengths present around the adsorption site. In a similar observation to the $\alpha\text{-Mg}_3(\text{HCO}_2)_6$ system, the thermal ellipsoid of the methane carbon atom in $\alpha\text{-Zn}_3(\text{HCO}_2)_6$ stretches and points toward the adjacent symmetry-equivalent methane carbon atom (Figure S3 b in the Supporting Information), implying that methane rapidly moves between the adjacent adsorption sites located along the channels.

The closest framework atom to the position of the adsorbed CH₃D carbon atom is a carbon atom on the formate linker located 3.731 Å away (Figure 1 f). The CH₃D carbon atom is also found 3.753 Å away from the oxygen atom of the formate linker, which is part of the ZnO₆ octahedron with the Zn3 atom located at the center (Figure 1 f), hinting at an interaction between the formate oxygen atom and the methane molecule. The aforementioned interatomic distances in α -Zn₃(HCO₂)₆ are relatively shorter than the 3.814 Å methane carbon atom–framework oxygen atom and 3.799 Å methane carbon atom–framework carbon atom distances within α -Mg₃(HCO₂)₆, which is in good agreement with a prior DFT computational study that indicated that α -Zn₃(HCO₂)₆ possesses a higher methane binding strength versus α -Mg₃(HCO₂)₆.^[35] The α -Mg₃(HCO₂)₆ and α -Zn₃(HCO₂)₆ MOFs feature fully saturated metal centers and have the same topology as well as organic linker, thus, any changes in the adsorption strength cannot be directly related to the nature of the metal center.

DFT geometry optimizations and calculations based on our SCXRD structure were performed to investigate the methane adsorption energy. The calculated adsorption energy of methane within α -Zn₃(HCO₂)₆ at a loading level of 1.0 methane per unit cell is -27.9 kJ mol⁻¹ (Table S1 in the Supporting Information), which is quite similar to the value of -27.6 kJ mol⁻¹ produced by previous DFT calculations.^[35] It is very interesting to note that the non-dispersive contribution in α -Zn₃(HCO₂)₆ is -5.3 kJ mol⁻¹ (Table S1 in the Supporting Information), which is only 0.5 kJ mol⁻¹ stronger than that of α -Mg₃(HCO₂)₆ (-4.8 kJ mol⁻¹), however, the dispersive contribution in α -Zn₃(HCO₂)₆ is -22.6 kJ mol⁻¹, which is 2.3 kJ mol⁻¹ stronger than that of α -Mg₃(HCO₂)₆ (Table S1 in the Supporting Information). These values reveal that the stronger methane binding strength in α -Zn₃(HCO₂)₆ is likely due to increased van der Waals interactions arising from the smaller pore size. The DFT geometry optimizations are shown from a long-range perspective in Figure S8 in the Supporting Information. Our SCXRD and DFT findings strongly support the notion that the pore size is the main determinant of the methane adsorption strength in this formate MOF family. To probe the effects of a reduced pore size on the methane binding strength, as well as to verify the presence of a single unique methane adsorption site, ²H SSNMR experiments were performed on α -Zn₃(HCO₂)₆.

²H SSNMR examination of methane within α -Zn₃(HCO₂)₆

Static VT ²H SSNMR experiments on singly-deuterated methane within α -Zn₃(HCO₂)₆ at a loading level of 0.1 CH₃D per Zn (1.2 CH₃D molecules per unit cell) were performed at temperatures ranging from 123 to 293 K (Figure 3 c). At 293 K, CH₃D is highly mobile within α -Zn₃(HCO₂)₆ and gives rise to a sharp resonance, and the ²H SSNMR spectra become steadily broader as the temperature decreases. At and below 173 K, the spectrum exhibits well-defined features and is composed of a single ²H powder pattern, reflecting the presence of a single crystallographically unique methane adsorption site in α -Zn₃(HCO₂)₆, which is in excellent agreement with the SCXRD and DFT results.

The observed C_Q(²H) values of CH₃D adsorbed within α -Zn₃(HCO₂)₆ increase from 500 Hz at 173 K to 920 Hz at 123 K (Table 1), yet these values are far less than the C_Q(²H) values of 192 kHz associated with static CH₃D. We are again observing a time-averaged ²H SSNMR spectrum involving fast exchange between isotropically tumbling CH₃D and adsorbed CH₃D moving anisotropically. The calculated C_Q(²H) value for a static methane molecule at the α -Zn₃(HCO₂)₆ methane adsorption site is also nearly identical to the NMR parameters for a single static CH₃D molecule (Table S2 in the Supporting Information), clearly indicating that time-averaged motional scaling of the QI must be responsible for the very small observed C_Q(²H) values. The increase in the observed C_Q(²H) values as the temperature is reduced reflects a decrease in the time-averaged methane mobility. The observed η_Q values increase from 0.20 to 0.50 as the temperature decreases from 173 to 123 K.

Much like the case of α -Mg₃(HCO₂)₆, the ²H powder patterns of adsorbed CH₃D in α -Zn₃(HCO₂)₆ are clearly influenced by the CSA that is not completely removed by methane motion (Table 1); this is reflected in the apparent span values of 2.0 ppm across the experimental temperature range. Although the anisotropy of the QI is largely removed by time-averaged CH₃D motion at low temperatures, a significant ²H CSA contribution in CH₃D remains. This ²H CSA contribution is again attributed to the NICS effect arising from the nearby MOF surface (see above). As the temperature is reduced, methane molecules remain in fast exchange but spend less time as isotropically tumbling free guests, and a larger fraction of time as adsorbed species undergoing slightly non-isotropic motions near the MOF surface and experiencing NICS effects. The net result is less time-averaged motional scaling of the CSA, making CSA effects more apparent in the ²H SSNMR spectra of fast-exchanging guest methane molecules in α -Zn₃(HCO₂)₆.

The VT ²H SSNMR spectral line shapes of CH₃D in both α -Zn₃(HCO₂)₆ and α -Mg₃(HCO₂)₆ are in the same realm, hinting that CH₃D has comparable mobility and adsorption energies in both systems. However, the ²H SSNMR spectra of CH₃D in α -Zn₃(HCO₂)₆ are broader than those of CH₃D in α -Mg₃(HCO₂)₆ at any given temperature, indicating that less of the CSA and QI anisotropy is removed, and thus methane is relatively less mobile and more strongly adsorbed in α -Zn₃(HCO₂)₆. This is supported by the observed NMR parameters given in Table 1: the methane C_Q(²H) values are 1–12% higher and the ²H span value is 250% higher in α -Zn₃(HCO₂)₆ versus α -Mg₃(HCO₂)₆ across the experimental temperature range. Further support for a decreased methane mobility in α -Zn₃(HCO₂)₆ comes from the DFT-calculated methane isosteric adsorption heats of -25.1 kJ mol⁻¹ in α -Mg₃(HCO₂)₆ and -27.9 kJ mol⁻¹ in α -Zn₃(HCO₂)₆ (Table S1 in the Supporting Information). The ²H SSNMR findings of stronger methane binding in α -Zn₃(HCO₂)₆ as compared to α -Mg₃(HCO₂)₆ are in agreement with the relatively shorter methane–framework distances in α -Zn₃(HCO₂)₆ indicated from our SCXRD and DFT computational results. The relatively larger magnitude of apparent ²H CSA in α -Zn₃(HCO₂)₆ is likely related to the pore size, because the pores are slightly smaller in this MOF and thus more methane guests are proximate to the MOF surfaces and experiencing

some degree of the NICS effect at any given time. It should also be noted that the ^2H δ_{iso} values decrease for deuterated methane adsorbed within $\alpha\text{-Zn}_3(\text{HCO}_2)_6$ as the temperature is reduced (Table 1). This is due to the fact that the time-averaged population of methane molecules adsorbed and located near the MOF surface increases at lower temperatures. To further investigate the behavior of methane adsorbed in small pore MOFs, the ultra-microporous MOF SIFSIX-3-Zn was examined.

Methane adsorption and dynamics within SIFSIX-3-Zn

SIFSIX-3-Zn is an ultra-microporous MOF well-suited for the selective adsorption of small gases,^[21d,44] for example, SIFSIX-3-Zn exhibits selective CO_2 capture in the presence of water.^[21d] SIFSIX-3-Zn also has a good methane adsorption capacity at low pressure (12.6 mg g^{-1} at 1 bar) due to the small pore size.^[21d] The name "SIFSIX" originates from the presence of pillared SiF_6^{2-} units within the MOF. In SIFSIX-3-Zn, the Zn^{II} center is saturated and octahedrally coordinated by four N atoms from four different pyrazine ligands, as well as two F atoms from two SiF_6^{2-} ions (Figure 5). The fluorine atoms are axially coordinated to Zn and the corresponding Zn–Zn axial distance is 7.6 \AA , whereas the four pyrazine linkers are equatorially coordinated to Zn, and the Zn–Zn equatorial distance is 7.1 \AA .^[45] The planes of the pyrazine linkers in SIFSIX-3-Zn are oriented parallel to the crystallographic c axis, producing square-shaped MOF channels measuring 3.8 \AA ^[21d,45] from corner to corner, which are significantly smaller than the calculated 4.58 and 4.44 \AA ^[35] pore sizes in $\alpha\text{-Mg}_3(\text{HCO}_2)_6$ and $\alpha\text{-Zn}_3(\text{HCO}_2)_6$, respectively. The very small pore size of SIFSIX-3-Zn bodes well for methane storage applications: because the interactions between methane molecules and MOFs are typically van der Waals (i.e., dispersive) interactions, the methane binding strength of a MOF should be enhanced as the pore size is reduced,^[6a,46] as was observed from DFT calculations and ^2H SSNMR experiments in the case of $\alpha\text{-Zn}_3(\text{HCO}_2)_6$ versus $\alpha\text{-Mg}_3(\text{HCO}_2)_6$ (see above). Despite the promising features that exist within the ultra-microporous SIFSIX-3-Zn for methane adsorption, a detailed study of the corresponding methane adsorption sites has not yet been performed. By using SCXRD,

DFT calculations, and VT ^2H SSNMR experiments, we now examine the methane adsorption sites and host–guest interactions in SIFSIX-3-Zn.

SCXRD and DFT calculations of SIFSIX-3-Zn loaded with methane

In order to locate the methane adsorption sites inside the channels of SIFSIX-3-Zn, SCXRD of SIFSIX-3-Zn saturated with CH_3D was performed at 110 K , yielding the crystal structure shown in Figure 5. When viewing the crystal structure along the c axis, the carbon atoms of CH_3D are located exactly in the middle of the MOF channels at a distance of 3.504 \AA from the closest framework atoms, which are the fluorine atoms of the SiF_6^{2-} linkers (Figures 5 a and b). This suggests that the fluorine atoms play an important role in the methane adsorption. Dispersive interactions in SIFSIX-3-Zn play a dominant role in the methane adsorption (see below), whereas non-dispersive mechanisms only play a minor role. The interatomic distances suggest that the relatively weaker non-dispersive interactions occur between the partially positive hydrogen atoms of the methane molecules and the negatively charged fluorine atoms of the SiF_6^{2-} linkers. The coordinatively saturated Zn centers are unable to directly interact with CH_3D .

The positions of the methane carbon atoms in SIFSIX-3-Zn are shown along the crystallographic a axis in Figure 5 c. This perspective clearly illustrates the two symmetry-equivalent adsorption sites per unit cell; however, there is only one crystallographically unique methane adsorption site. The distance between the two symmetry-equivalent CH_3D adsorption sites is only 1.944 \AA , which is much shorter than the approximately 5.4 \AA distance between adjacent methane adsorption sites in the MOFs $\alpha\text{-Mg}_3(\text{HCO}_2)_6$ and $\alpha\text{-Zn}_3(\text{HCO}_2)_6$. The short distance between adjacent CH_3D adsorption sites in SIFSIX-3-Zn means they cannot be simultaneously populated in the same unit cell, which is supported by the 0.38 molecules per unit cell occupancy of the methane carbon atom. The ORTEP diagram of methane in the asymmetric unit of SIFSIX-3-Zn highlights the very large thermal ellipsoid of the CH_3D carbon atom, along with its anisotropic elongation along the crystallographic c axis towards the adjacent adsorption site (Figures S9 and S3 c in

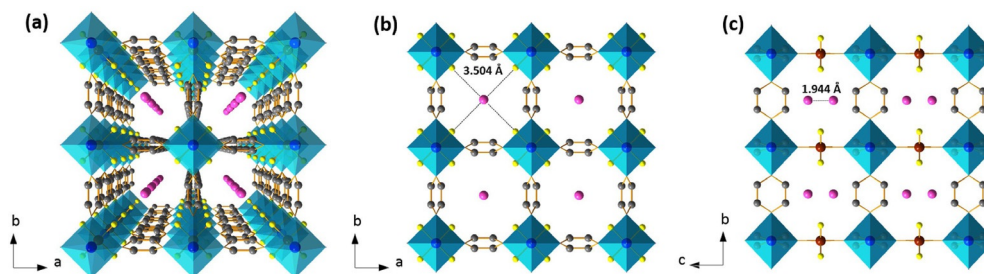


Figure 5. a) Long-range structure of SIFSIX-3-Zn as determined from our SCXRD experiments viewed along the crystallographic c axis, with the carbon atom positions of adsorbed CH_3D within the MOF pores illustrated in purple. b) The purple CH_3D carbon atom locations in one cross-section of the SIFSIX-3-Zn crystal structure are shown as viewed along the c axis, where the shortest distance between CH_3D carbon atoms and the framework (i.e., the fluorine atoms of SiF_6^{2-}) was measured as 3.504 \AA . c) Locations of the purple carbon atoms of CH_3D in SIFSIX-3-Zn, as viewed along the a axis, with the distance between the carbon atoms of adjacent adsorbed CH_3D molecules indicated as 1.944 \AA . In this illustration, carbon is colored gray, zinc is blue, silicon is brown, fluorine is yellow, nitrogen is light pink, and the carbon atoms of adsorbed CH_3D within SIFSIX-3-Zn are purple. Detailed information on the DFT optimized methane-loaded SIFSIX-3-Zn structure can be found in Figure S10 in the Supporting Information.

the Supporting Information). The large ellipsoid and its shape confirms that methane is remarkably mobile between the equivalent adsorption sites, even at 110 K.

The DFT-optimized adsorption site (Figure S10a in the Supporting Information) and the adsorption site determined by using SCXRD are located 0.98 Å apart. Nonetheless, the DFT-optimized methane adsorption site is located very close to the methane carbon ellipsoid obtained by using XRD, and these two complementary techniques generally are in good agreement. The calculated adsorption energy is $-33.3 \text{ kJ mol}^{-1}$ (Table S1 in the Supporting Information), which indicates that SIFSIX-3-Zn has a significantly stronger methane binding strength over both $\alpha\text{-Mg}_3(\text{HCO}_2)_6$ and $\alpha\text{-Zn}_3(\text{HCO}_2)_6$. Based on DFT optimizations, the methane hydrogen atoms make distant 2.5–3.4 Å contacts with the framework fluorine atoms; these non-dispersive contributions are calculated to contribute only -0.6 kJ mol^{-1} to the guest adsorption (Table S1 in the Supporting Information), which indicates that the electrostatic H–F interaction is quite weak. In contrast, the dispersive adsorption contribution was found to be $-32.7 \text{ kJ mol}^{-1}$ (Table S1 in the Supporting Information), which is a clear indication that the relatively stronger methane binding strength in SIFSIX-3-Zn chiefly arises from its remarkably small pore size. In order to understand the effect of these narrower pores and stronger host–guest interactions on the local electronic and magnetic structure of adsorbed methane, static VT ^2H SSNMR experiments were performed.

^2H SSNMR examination of methane within SIFSIX-3-Zn

The static VT ^2H SSNMR spectra obtained at temperatures ranging from 123 to 293 K are shown in Figure 6a. At 293 K, the spectrum consists of a sharp resonance along with a relatively broader powder pattern that exhibits some spectral features (Figure 6a). The sharp narrow resonance corresponds to CH_3D that is isotropically tumbling within SIFSIX-3-Zn, and this signal decreases in intensity with the temperature until the sharp line is not visible at or below 213 K. Similar to the case of methane in $\alpha\text{-Mg}_3(\text{HCO}_2)_6$ and $\alpha\text{-Zn}_3(\text{HCO}_2)_6$, the broader underlying time-averaged ^2H powder pattern arises from CH_3D undergoing motional averaging. The observation of a single ^2H SSNMR powder pattern indicates that there is only one crystallographically unique methane adsorption site in SIFSIX-3-Zn, which is in good agreement with our SCXRD experiments and DFT optimizations.

The observed $C_Q(^2\text{H})$ value of CH_3D adsorbed within SIFSIX-3-Zn is 1520 Hz at 213 K, and this value increases as the temperature decreases, reaching 3700 Hz at 123 K (Table 1). The observed $C_Q(^2\text{H})$ values associated with CH_3D in SIFSIX-3-Zn remain far less than either the 192 kHz^[36] value for static methane or the calculated $C_Q(^2\text{H})$ value of approximately 190 kHz for static methane at the geometry-optimized SCXRD adsorption site (Table S2 in the Supporting Information), indicating that time-averaged CH_3D motion must be removing much of the QI anisotropy. However, the observed time-averaged motionally scaled $C_Q(^2\text{H})$ values of methane within SIFSIX-3-Zn are significantly larger than those of methane within the MOFs $\alpha\text{-Mg}_3(\text{HCO}_2)_6$

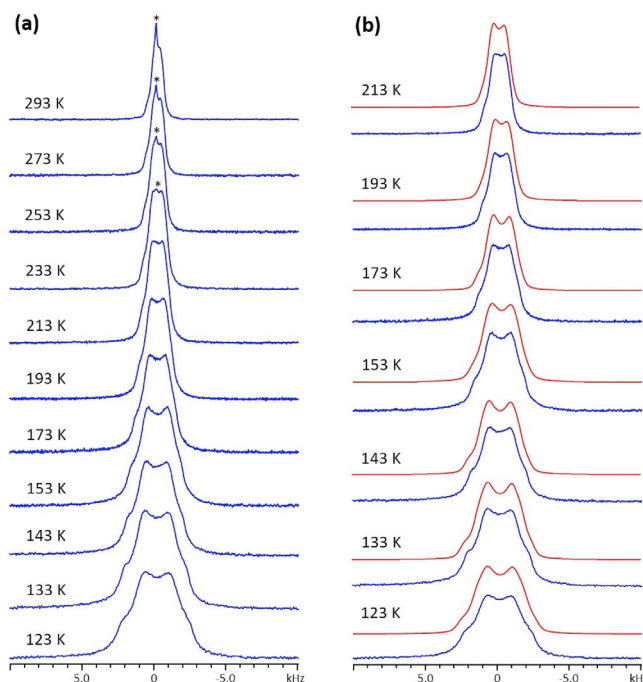


Figure 6. a) Experimental static VT ^2H SSNMR spectra of CH_3D adsorbed within SIFSIX-3-Zn. b) Comparison of the experimental (blue) and simulated (red) low-temperature ^2H SSNMR spectra of CH_3D in SIFSIX-3-Zn. The asterisk in a) denotes the sharp central ^2H resonance arising from non-adsorbed CH_3D undergoing rapid isotropic tumbling.

and $\alpha\text{-Zn}_3(\text{HCO}_2)_6$ at any given temperature, indicating that there is a larger fraction of methane molecules undergoing non-isotropic motion, and thus, there are stronger host–guest interactions within SIFSIX-3-Zn. This SSNMR spectroscopy-based conclusion is strongly supported by the relatively larger calculated adsorption energy of methane in SIFSIX-3-Zn versus $\alpha\text{-Mg}_3(\text{HCO}_2)_6$ and $\alpha\text{-Zn}_3(\text{HCO}_2)_6$ (see above, Table S1 in the Supporting Information). The ^2H SSNMR spectra and DFT calculations of these three MOFs reveal a clear link between increased CH_3D $C_Q(^2\text{H})$ values and a reduced methane mobility.

Even with the increased QI and relatively broader time-averaged ^2H SSNMR powder patterns of CH_3D in SIFSIX-3-Zn, the spectral line shape is significantly influenced by the CSA. The observed Ω value is 2.5 ppm at all temperatures, which is larger than the 2.0 and 0.8 ppm values in $\alpha\text{-Zn}_3(\text{HCO}_2)_6$ and $\alpha\text{-Mg}_3(\text{HCO}_2)_6$, respectively. Much like the case of the $C_Q(^2\text{H})$ values, it appears that larger Ω values are linked to smaller pore sizes and stronger methane binding in these three MOFs. We believe that this elevated span value arises from a relatively larger NICS effect; stronger host–guest interactions cause a significantly larger fraction of methane molecules to be adsorbed near the SIFSIX-3-Zn surface and thus, subject to the NICS at any given time. The ^2H δ_{iso} value of CH_3D adsorbed in SIFSIX-3-Zn is -2.0 ppm at temperatures ranging from 213 to 123 K (Table 1), which is much larger in magnitude than the -0.2 to -0.7 ppm values observed for CH_3D in $\alpha\text{-Zn}_3(\text{HCO}_2)_6$ and $\alpha\text{-Mg}_3(\text{HCO}_2)_6$, respectively. The larger magnitude of the observed

δ_{180} value again indicates a stronger NICS effect on methane in SIFSIX-3-Zn.

The β parameter denotes the angle between the V_{33} component of the ^2H EFG tensor and the δ_{33} component of the ^2H CS tensor. Interestingly, the observed β value for adsorbed CH_3D is 80° in SIFSIX-3-Zn, but it is 0° in $\alpha\text{-Mg}_3(\text{HCO}_2)_6$ and $\alpha\text{-Zn}_3(\text{HCO}_2)_6$. DFT calculations for all four ^2H positions on adsorbed methane in $\alpha\text{-Mg}_3(\text{HCO}_2)_6$ and $\alpha\text{-Zn}_3(\text{HCO}_2)_6$, along with three of four ^2H positions for adsorbed methane in SIFSIX-3-Zn, predict β values close to 0° (Table S2 in the Supporting Information). Thus, it appears that the ^2H V_{33} and/or δ_{33} tensor components have been reoriented for CH_3D adsorbed in SIFSIX-3-Zn. For terminally bound ^2H atoms, it is known that the V_{33} component of the EFG tensor is almost always located along the direction of the single chemical bond, and there are no indications from SCXRD or DFT that significant hydrogen-bonding interactions or additional chemical bonds involving methane H/D atoms that may reorient the V_{33} component are present within the SIFSIX-3-Zn framework. Thus, the most likely scenario is that the δ_{33} component of the CS tensor has been reoriented to produce the observed β value of 80° . Based on the relatively strong NICS influence on the ^2H CSA parameters in SIFSIX-3-Zn, we suggest that the NICS may also be responsible for the change in the β value: the NICS significantly alters the ^2H CS tensor orientation of deuterium atoms on adsorbed methane molecules located close to the internal surfaces of SIFSIX-3-Zn, rendering the CH_3D ^2H CS and EFG tensors nearly perpendicular rather than coincident.

SIFSIX-3-Zn, $\alpha\text{-Mg}_3(\text{HCO}_2)_6$, and $\alpha\text{-Zn}_3(\text{HCO}_2)_6$ all feature saturated metal centers that cannot directly interact with methane guests. However, in many MOFs, the presence of a coordinatively unsaturated open metal site (OMS) facilitates guest gas adsorption and can boost the total adsorption capacity. In order to investigate the influence of OMSs on the methane adsorption and the ^2H SSNMR spectra, the framework M-MOF-74 was examined.

^2H SSNMR of methane adsorbed within M-MOF-74

M-MOF-74 (M = Mg, Zn, Ni, Co) is a MOF consisting of metal centers joined by 2,5-dioxido-1,4-benzenedicarboxylate (dobdc) linkers, forming a framework that features hexagonal or honeycomb-shaped channels that have metal centers at each vertex with a metal–metal distance of approximately 9 \AA .^[21c,47] In the as-made version of MOF-74, each metal center is connected to five oxygen atoms from four dobdc linkers and a sixth oxygen atom from a solvent molecule originating from the synthesis, such as tetrahydrofuran. The coordinated solvent molecules can then be removed through activation (i.e., heating and vacuum) to create coordinatively unsaturated OMSs, which are accessible to guests within the pores and thus act as the adsorption sites for guest gases, such as methane.^[12b] The nature of the metal center influences the methane binding strength, which has been found to follow the order $\text{Ni} > \text{Co} > \text{Mg} > \text{Zn}$.^[1a,12b,48] In M-MOF-74, the adsorbed methane molecule is located near the OMS (i.e., adjacent to the base of the MO_5 square pyramid) in order to maximize the host–guest interac-

tions.^[12b] Although the locations of adsorbed methane in these systems are known,^[12b] the host–guest interactions between methane and M-MOF-74 have not yet been explored using SSNMR methods.

The VT ^2H SSNMR spectra of CH_3D within the diamagnetic Mg-MOF-74 are shown in Figure 7. At 293 K, only a single sharp, narrow resonance corresponding to highly mobile, isotropically tumbling CH_3D is observed. The ^2H SSNMR resonance

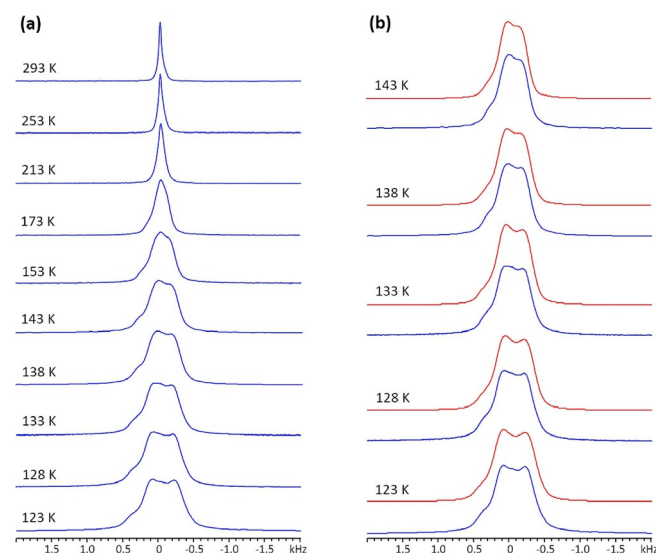


Figure 7. a) Experimental static VT ^2H SSNMR spectra of CH_3D adsorbed in Mg-MOF-74. b) Comparison of the experimental (blue) and simulated (red) low-temperature ^2H SSNMR spectra.

grows gradually broader as the temperature decreases, reflecting a reduction in the time-averaged CH_3D dynamics. A well-defined and relatively broader ^2H powder pattern indicative of adsorbed methane is only observed at and below 143 K, which is a lower temperature compared with the other MOFs within this study; this finding suggests that Mg-MOF-74 has a weaker methane binding strength than $\alpha\text{-Mg}_3(\text{HCO}_2)_6$, $\alpha\text{-Zn}_3(\text{HCO}_2)_6$, and SIFSIX-3-Zn (see below).

The observed ^2H NMR parameters for methane adsorbed in Mg-MOF-74 at and below 143 K are listed in Table 1. The observed $C_Q(^2\text{H})$ values are relatively small and increase from 420 Hz at 143 K to 620 Hz at 123 K. Because these $C_Q(^2\text{H})$ values are much less than the known static value of 192 kHz, it is again apparent that we are observing a time-averaged ^2H SSNMR spectrum arising from CH_3D tumbling in the pore undergoing a fast exchange with CH_3D interacting with the surface in M-MOF-74. The observed $C_Q(^2\text{H})$ values are lower than those of $\alpha\text{-Mg}_3(\text{HCO}_2)_6$, $\alpha\text{-Zn}_3(\text{HCO}_2)_6$, and SIFSIX-3-Zn at any given temperature, strongly suggesting that Mg-MOF-74 has the weakest methane binding strength of the four. This observation is in good agreement with a previous study that indicated that Mg-MOF-74 has an isosteric heat of methane adsorption of $-18.5 \text{ kJ mol}^{-1}$,^[12b] which is significantly lower than that of $\alpha\text{-Mg}_3(\text{HCO}_2)_6$ ($-25.1 \text{ kJ mol}^{-1}$), $\alpha\text{-Zn}_3(\text{HCO}_2)_6$ ($-27.9 \text{ kJ mol}^{-1}$), and SIFSIX-3-Zn ($-33.3 \text{ kJ mol}^{-1}$) calculated in

this work (Table S1 in the Supporting Information). These data again suggest that increased $C_Q(^2\text{H})$ values can be linked to a decreased methane mobility in these MOFs. The ^2H powder patterns are distorted from purely QI-dominated line shapes due to the presence of CSA that is not wholly removed by rapid guest motion (Table 1). Much like the previously discussed $\alpha\text{-Mg}_3(\text{HCO}_2)_6$, $\alpha\text{-Zn}_3(\text{HCO}_2)_6$, and SIFSIX-3-Zn, there appears to be an observable NICS contribution to the ^2H CSA of methane in Mg-MOF-74, as evidenced by the negative ^2H δ_{iso} value of -0.8 ppm and the ^2H span value of 2.0 ppm throughout the experimental temperature range.

The VT ^2H SSNMR spectra of CH_3D adsorbed within Zn-MOF-74 were also obtained, and the low-temperature spectra are shown in Figure 8a. Throughout the temperature range, the ^2H SSNMR spectrum features only a single sharp resonance, corresponding to highly mobile and isotropically tumbling CH_3D molecules. This observation is surprising, given that the methane binding strength in Zn-MOF-74 (isosteric heat of adsorption: -18.3 kJ mol^{-1}) is very similar to that of Mg-MOF-74 (isosteric heat of adsorption: -18.5 kJ mol^{-1}).^[12b] This is an apparent exception to the link we have observed between higher $C_Q(^2\text{H})$ values (i.e., broader powder patterns), increased isosteric heats of adsorption, and reduced methane mobility for all other MOFs up to this point. A possible explanation comes from the calculated binding energy of methane on the Zn^{2+} OMSs at 0 K of 29.7 kJ mol^{-1} , which is 4.1 kJ mol^{-1} lower than that on Mg^{2+} OMSs,^[12b] this difference may lead to increased methane mobility and explain why a featureless ^2H resonance was observed in CH_3D -loaded Zn-MOF-74. Another

possible reason for the differences in the binding strength between Mg-MOF-74 and Zn-MOF-74 is the relatively stronger repulsive interaction between the Zn-MOF-74 framework and methane, which leads to a weaker methane binding strength in Zn-MOF-74.^[49]

Ni-MOF-74 (isosteric heat of adsorption: -20.2 kJ mol^{-1}) and Co-MOF-74 (isosteric heat of adsorption: -19.6 kJ mol^{-1}) exhibit stronger methane binding strengths versus Mg-MOF-74 and Zn-MOF-74,^[12b] however, the paramagnetic Ni^{2+} and Co^{2+} centers in MOF-74 present a unique challenge for ^2H SSNMR experiments. When a CH_3D guest is proximate to these paramagnetic metal centers, the large magnetic moment of the unpaired electrons in Ni^{2+} and Co^{2+} couples with the ^2H nucleus in CH_3D , resulting in spectral broadening and unusual chemical shifts. The VT ^2H SSNMR spectra of CH_3D adsorbed within Ni-MOF-74 and Co-MOF-74 are shown in Figures 8b and c. At 373 K, the ^2H SSNMR spectra of adsorbed CH_3D within Ni-MOF-74 and Co-MOF-74 exhibit a single resonance with a full width at half height (FWHH) of 3.3 and 12.2 kHz, respectively. This pronounced spectral broadening confirms that CH_3D is located close to the paramagnetic open metal sites (i.e., CH_3D is proximate to or physically adsorbed on the OMS). The broad ^2H resonance in Ni-MOF-74 and Co-MOF-74 increases in width as the temperature is reduced, and the resonances are gradually shifted to higher and lower frequencies, respectively. The increases in the resonance width and the magnitude of frequency shifts are indicative of increasingly stronger interactions between the CH_3D guests and the paramagnetic OMSs as the temperature is reduced; this agrees with the common observation of an in-

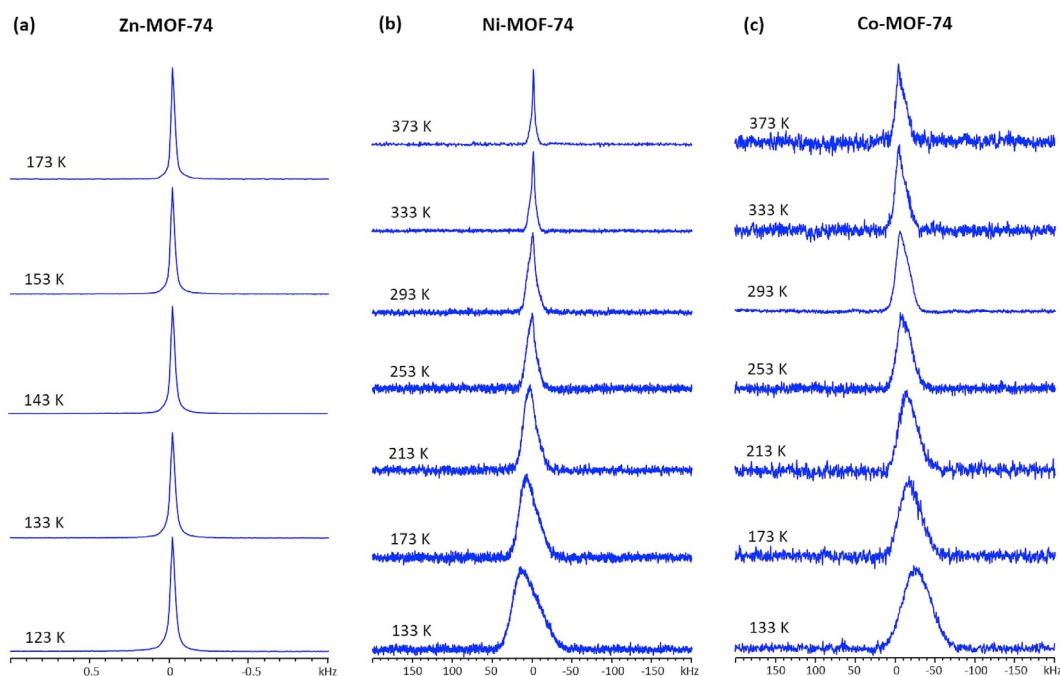


Figure 8. Experimental static VT ^2H SSNMR spectra of CH_3D adsorbed within a) Zn-MOF-74, b) Ni-MOF-74, and c) Co-MOF-74 at a loading level of 0.2 CH_3D per metal center. Note the difference in the x-axis scale between a), b), and c). The spectral broadening and apparent change in the isotropic chemical shifts observed in Ni-MOF-74 and Co-MOF-74 are due to the presence of paramagnetic metal centers and the corresponding coupling between the paramagnetic metal center and the deuterium nucleus in CH_3D . In Ni-MOF-74, the most intense point of the ^2H resonance shifts from -1.4 kHz at 373 K to 12.0 kHz at 133 K, for a total frequency shift of approximately 13.5 kHz. In Co-MOF-74, the position of the most intense point of the ^2H resonance shifts from -4.7 kHz at 373 K to -26.3 kHz at 133 K, for a total frequency shift of about 22 kHz.

creased methane localization on the adsorption site as the temperature is reduced for all other MOFs within this study. It is very interesting to note that even though Ni-MOF-74 has a stronger methane binding strength than Co-MOF-74,^[12b] the ²H resonance width of CH₃D within Ni-MOF-74 is narrower than that of CH₃D within Co-MOF-74 at any given temperature (Figure 8b and c), despite the differences in the methane–metal proximity. It appears that the paramagnetic interaction has a more pronounced impact on the ²H SSNMR spectrum of CH₃D in Co-MOF-74 versus that of CH₃D within Ni-MOF-74, which is logical given that Co exhibits a magnetic moment larger than that of Ni in the MOF-74 system.^[50]

Comparison of the ²H SSNMR spectra of CH₃D, CH₂D₂, and CD₄

The VT ²H SSNMR spectra of CH₂D₂ and CD₄ adsorbed in α-Mg₃(HCO₂)₆ (Figures S11a and b in the Supporting Information), α-Zn₃(HCO₂)₆ (Figure S11c and d in the Supporting Information), and Mg-MOF-74 (Figure S13 in the Supporting Information), along with those of CH₂D₂ adsorbed in SIFSIX-3-Zn (Figure S12 in the Supporting Information) were also acquired to investigate the effect of different deuteration patterns on the host–guest interactions, the ²H SSNMR spectra, and the associated ²H NMR parameters (Table S4 in the Supporting Information) within these MOFs. A stacked illustration of the CH₃D, CH₂D₂, and CD₄ ²H SSNMR spectra is provided in Figure S14 in the Supporting Information. Each deuteration pattern produced a unique ²H spectrum; there is a more detailed discussion of this data within the Supporting Information.

Conclusions

The combination of SCXRD, DFT calculations, and ²H SSNMR experiments has revealed rich insights regarding the methane adsorption and mobility in metal–organic frameworks α-Mg₃(HCO₂)₆, α-Zn₃(HCO₂)₆, SIFSIX-3-Zn, and MOF-74.

SCXRD experiments were able to unambiguously locate the single crystallographically unique methane adsorption site within α-Mg₃(HCO₂)₆, α-Zn₃(HCO₂)₆, and SIFSIX-3-Zn at these guest loading levels. In α-Mg₃(HCO₂)₆ and α-Zn₃(HCO₂)₆, the adsorption site is located proximate to a carbon and an oxygen atom of the formate linkers, whereas in SIFSIX-3-Zn, the adsorbed methane molecules are positioned in the center of the channel. In all MOFs, the thermal ellipsoid of the methane carbon atom is quite large, reflecting a high degree of methane mobility. DFT calculations produced the geometry-optimized position of methane in these MOF structures, which were found to be in good agreement with the SCXRD experimental results. The calculations indicate that the methane adsorption is driven mainly by dispersive forces within these MOFs, which were found to be inversely related to the pore size. The calculated total adsorption energies follow the order SIFSIX-3-Zn (−33.3 kJ mol^{−1}) > α-Zn₃(HCO₂)₆ (−27.9 kJ mol^{−1}) > α-Mg₃(HCO₂)₆ (−25.1 kJ mol^{−1}).

Static VT ²H SSNMR experiments of singly deuterated CH₃D guests confirmed that only one crystallographically unique

methane adsorption site exists in each MOF at the experimental guest loading levels. The ²H SSNMR spectral appearance originates from the time-averaged combination of two methane species in fast exchange, that is, methane isotropically tumbling in the MOF pores, and adsorbed methane moving in an anisotropic manner as it interacts with the MOF surface. The ²H SSNMR spectral appearance of CH₃D in these MOFs is primarily determined by the ²H QI, which is significantly reduced by the methane motion. Increases in the observed C_Q(²H) values are strongly correlated to increases in the methane binding strength within all four MOFs studied. Interestingly, the ²H CSA is not completely eliminated by motional averaging as expected. Instead, the CSA actually makes a significant contribution to the ²H spectral appearance; we propose that the NICS effect in guest-loaded MOFs re-introduces an observable amount of ²H CSA to the adsorbed methane molecules located near the MOF surface. The methane binding strength is linked to the magnitude of the NICS effect. ²H SSNMR experiments of CH₃D adsorbed at the OMSs in Mg-MOF-74 and Zn-MOF-74 confirm that Mg-MOF-74 has a stronger methane binding ability than Zn-MOF-74. For CH₃D adsorbed in Co-MOF-74 and Ni-MOF-74, the ²H SSNMR spectra are broadened by interactions between the paramagnetic metal centers and the methane deuterium nuclei, with NMR parameters unavailable from the broad, featureless spectra.

This work illustrates how large amounts of high-quality data regarding methane adsorption sites, host–guest interactions, guest mobility, and guest deuteration can be obtained when using a combination of SCXRD, DFT, and SSNMR methods. By employing this characterization strategy, methane adsorption may now be extensively investigated within other MOFs and porous materials, and the knowledge obtained from this investigative approach should prove very helpful for the development of novel MOFs and porous materials for methane adsorption.

Acknowledgements

Y.H. thanks the Natural Science and Engineering Research Council (NSERC) of Canada for a Discovery Grant and a Discovery Accelerator Supplements Award. M.F. is grateful to Prof. Dr. Andreas Lüttge and Dr. Rolf Arvidson (Marum, Bremen) for generous access to the Asgard cluster, on which the DFT calculations were run. Funding of M.F. was provided by the Central Research Development Fund (CRDF) of the University of Bremen (Funding line 04: Independent Projects for Post Docs). A portion of the computations were performed by using resources provided by the North-German Supercomputing Alliance (HLRN). The authors thank Dr. V. V. Terskikh (University of Ottawa) for his assistance.

Conflict of interest

The authors declare no conflict of interest.

Keywords: adsorption · density functional calculations · host-guest systems · microporous materials · NMR spectroscopy · X-ray diffraction

- [1] a) J. A. Mason, M. Veenstra, J. R. Long, *Chem. Sci.* **2014**, *5*, 32–51; b) R. F. Service, *Science* **2014**, *346*, 538–541.
- [2] a) Alternative Fuels Data Center: Fuel Properties Comparison, **2013**, http://www.afdc.energy.gov/fuels/fuel_comparison_chart.pdf; b) G. A. Whyatt, Issues Affecting Adoption of Natural Gas Fuel in Light- and Heavy-Duty Vehicles. Report No. PNNL-19745 (US Department of Energy, 2010).
- [3] a) T. A. Makal, J.-R. Li, W. Lu, H.-C. Zhou, *Chem. Soc. Rev.* **2012**, *41*, 7761–7779; b) K. V. Kumar, K. Preuss, M.-M. Titirici, F. Rodríguez-Reinoso, *Chem. Rev.* **2017**, *117*, 1796–1825.
- [4] a) Advanced Research Projects Agency: Energy. Methane Opportunities for Vehicular Energy (Funding opportunity no. De-FOA-0000672, US Department of Energy, **2012**); b) C. M. Simon, J. Kim, D. A. Gomez-Gualdrón, J. S. Camp, Y. G. Chung, R. L. Martin, R. Mercado, M. W. Deem, D. Gunter, M. Haranczyk, D. S. Sholl, R. Q. Snurr, B. Smit, *Energy Environ. Sci.* **2015**, *8*, 1190–1199.
- [5] a) S. L. James, *Chem. Soc. Rev.* **2003**, *32*, 276–288; b) H.-C. Zhou, S. Kitagawa, *Chem. Soc. Rev.* **2014**, *43*, 5415–5418; c) H.-C. Zhou, J. R. Long, O. M. Yaghi, *Chem. Rev.* **2012**, *112*, 673–674.
- [6] a) B. Li, H.-M. Wen, W. Zhou, B. Chen, *J. Phys. Chem. Lett.* **2014**, *5*, 3468–3479; b) S. Ma, H.-C. Zhou, *Chem. Commun.* **2010**, *46*, 44–53.
- [7] a) Y. He, W. Zhou, G. Qian, B. Chen, *Chem. Soc. Rev.* **2014**, *43*, 5657–5678; b) K. Konstantis, T. Osl, Y. Yang, M. Batten, N. Burke, A. J. Hill, M. R. Hill, *J. Mater. Chem.* **2012**, *22*, 16698–16708.
- [8] J. A. Mason, J. Oktawiec, M. K. Taylor, M. R. Hudson, J. Rodriguez, J. E. Bachman, M. I. Gonzalez, A. Cervellino, A. Guagliardi, C. M. Brown, P. L. Llewellyn, N. Masciocchi, J. R. Long, *Nature* **2015**, *527*, 357–361.
- [9] M. Gaab, N. Trukhan, S. Maurer, R. Gummaraju, U. Müller, *Microporous Mesoporous Mater.* **2012**, *157*, 131–136.
- [10] Y. Peng, V. Krungleviciute, I. Eryazici, J. T. Hupp, O. K. Farha, T. Yildirim, *J. Am. Chem. Soc.* **2013**, *135*, 11887–11894.
- [11] E. J. Carrington, I. J. Vitorica-Yrezabal, L. Brammer, *Acta Crystallogr. Sect. B* **2014**, *70*, 404–422.
- [12] a) J. Getzschmann, I. Senkowska, D. Wallacher, M. Tovar, D. Fairen-Jimenez, T. Düren, J. M. van Baten, R. Krishna, S. Kaskel, *Microporous Mesoporous Mater.* **2010**, *136*, 50–58; b) H. Wu, W. Zhou, T. Yildirim, *J. Am. Chem. Soc.* **2009**, *131*, 4995–5000; c) H. Wu, W. Zhou, T. Yildirim, *J. Phys. Chem. C* **2009**, *113*, 3029–3035.
- [13] a) H. Kim, D. G. Samsonenko, S. Das, G.-H. Kim, H.-S. Lee, D. N. Dybtsev, E. A. Berdonosova, K. Kim, *Chem. Asian J.* **2009**, *4*, 886–891; b) S. R. Miller, P. A. Wright, T. Devic, C. Serre, G. Férey, P. L. Llewellyn, R. Denoyel, L. Gabetova, Y. Filinchuk, *Langmuir* **2009**, *25*, 3618–3626; c) S. Chen, B. E. G. Lucier, P. D. Boyle, Y. Huang, *Chem. Mater.* **2016**, *28*, 5829–5846.
- [14] a) P. L. Llewellyn, P. Horcajada, G. Maurin, T. Devic, N. Rosenbach, S. Bourrelly, C. Serre, D. Vincent, S. Loera-Serna, Y. Filinchuk, G. Férey, *J. Am. Chem. Soc.* **2009**, *131*, 13002–13008; b) N. A. Ramsahye, T. K. Trung, S. Bourrelly, Q. Yang, T. Devic, G. Maurin, P. Horcajada, P. L. Llewellyn, P. Yot, C. Serre, Y. Filinchuk, F. Fajula, G. Férey, P. Trens, *J. Phys. Chem. C* **2011**, *115*, 18683–18695.
- [15] a) R. B. Getman, Y.-S. Bae, C. E. Wilmer, R. Q. Snurr, *Chem. Rev.* **2012**, *112*, 703–723; b) D. A. Gomez-Gualdrón, O. V. Gutov, V. Krungleviciute, B. Borah, J. E. Mondloch, J. T. Hupp, T. Yildirim, O. K. Farha, R. Q. Snurr, *Chem. Mater.* **2014**, *26*, 5632–5639.
- [16] a) Y. Huang, J. Xu, F. Gul-E-Noor, P. He in *Metal–Organic Frameworks: NMR Studies of Quadrupolar Nuclei*, Wiley, New York, **2011**; b) H. C. Hoffmann, M. Debowski, P. Muller, S. Paasch, I. Senkowska, S. Kaskel, E. Brunner, *Materials* **2012**, *5*, 2537–2572; c) A. Sutrisno, Y. Huang, *Solid State Nucl. Magn. Reson.* **2013**, *49–50*, 1–11; d) S. E. Ashbrook, D. M. Dawson, V. R. Seymour, *Phys. Chem. Chem. Phys.* **2014**, *16*, 8223–8242; e) P. He, B. E. G. Lucier, V. V. Tersikh, Q. Shi, J. Dong, Y. Chu, A. Zheng, A. Sutrisno, Y. Huang, *J. Phys. Chem. C* **2014**, *118*, 23728–23744; f) G. Mali, in *Looking into Metal–Organic Frameworks with Solid-State NMR Spectroscopy*, InTech, London, **2016**; g) R. Giovine, C. Volkringer, S. E. Ashbrook, J. Trébossé, D. McKay, T. Loiseau, J.-P. Amoureux, O. Lafon, F. Pourpoint, *Chem. Eur. J.* **2017**, *23*, 9525–9534; h) J. Xu, E. S. M. Blaakmeer, A. S. Lipton, T. M. McDonald, Y. M. Liu, B. Smit, J. R. Long, A. P. M. Kentgens, J. A. Reimer, *J. Phys. Chem. C* **2017**, *121*, 19938–19945.
- [17] a) X. Q. Kong, E. Scott, W. Ding, J. A. Mason, J. R. Long, J. A. Reimer, *J. Am. Chem. Soc.* **2012**, *134*, 14341–14344; b) L.-C. Lin, J. Kim, X. Kong, E. Scott, T. M. McDonald, J. R. Long, J. A. Reimer, B. Smit, *Angew. Chem. Int. Ed.* **2013**, *52*, 4410–4413; *Angew. Chem.* **2013**, *125*, 4506–4509; c) W. D. Wang, B. E. G. Lucier, V. V. Tersikh, W. Wang, Y. Huang, *J. Phys. Chem. Lett.* **2014**, *5*, 3360–3365; d) B. E. G. Lucier, H. Chan, Y. Zhang, Y. Huang, *Eur. J. Inorg. Chem.* **2016**, 2017–2024; e) B. E. G. Lucier, Y. Zhang, K. J. Lee, Y. Lu, Y. Huang, *Chem. Commun.* **2016**, *52*, 7541–7544; f) J. Xu, R. Sinelnikov, Y. Huang, *Langmuir* **2016**, *32*, 5468–5479; g) Y. Zhang, B. E. G. Lucier, Y. Huang, *Phys. Chem. Chem. Phys.* **2016**, *18*, 8327–8341; h) Y. Lu, B. E. G. Lucier, Y. Zhang, P. Ren, A. Zheng, Y. Huang, *Phys. Chem. Chem. Phys.* **2017**, *19*, 6130–6141.
- [18] R. L. Vold, G. L. Hoatson, *J. Magn. Reson.* **2009**, *198*, 57–72.
- [19] a) J. Gonzalez, R. N. Devi, D. P. Tunstall, P. A. Cox, P. A. Wright, *Microporous Mesoporous Mater.* **2005**, *84*, 97–104; b) S. L. Gould, D. Tranchemontagne, O. M. Yaghi, M. A. Garcia-Garibay, *J. Am. Chem. Soc.* **2008**, *130*, 3246–3247; c) D. I. Kolokolov, H. Jobic, A. G. Stepanov, V. Guillermt, T. Devic, C. Serre, G. Férey, *Angew. Chem. Int. Ed.* **2010**, *49*, 4791–4794; *Angew. Chem.* **2010**, *122*, 4901–4904; d) J. P. S. Mowat, S. R. Miller, J. M. Griffin, V. R. Seymour, S. E. Ashbrook, S. P. Thompson, D. Fairen-Jimenez, A.-M. Banu, T. Düren, P. A. Wright, *Inorg. Chem.* **2011**, *50*, 10844–10858; e) V. N. Vukotic, K. J. Harris, K. Zhu, R. W. Schurko, S. J. Loeb, *Nat. Chem.* **2012**, *4*, 456–460; f) D. I. Kolokolov, A. G. Stepanov, H. Jobic, *J. Phys. Chem. C* **2014**, *118*, 15978–15984.
- [20] a) T. Ueda, K. Kurokawa, H. Omichi, K. Miyakubo, T. Eguchi, *Chem. Phys. Lett.* **2007**, *443*, 293–297; b) S. Burekaew, S. Horike, M. Higuchi, M. Mizuno, T. Kawamura, D. Tanaka, N. Yanai, S. Kitagawa, *Nat. Mater.* **2009**, *8*, 831–836; c) D. I. Kolokolov, H. Jobic, S. Rives, P. G. Yot, J. Ollivier, P. Trens, A. G. Stepanov, G. Maurin, *J. Phys. Chem. C* **2015**, *119*, 8217–8225.
- [21] a) J. A. Rood, B. C. Noll, K. W. Henderson, *Inorg. Chem.* **2006**, *45*, 5521–5528; b) Z. Wang, Y. Zhang, M. Kurmoo, T. Liu, S. Vilminot, B. Zhao, S. Gao, *Aust. J. Chem.* **2006**, *59*, 617–628; c) P. D. C. Dietzel, R. Blom, H. Fjellvåg, *Eur. J. Inorg. Chem.* **2008**, 3624–3632; d) P. Nugent, Y. Belmabkhout, S. D. Burd, A. J. Cairns, R. Luebke, K. Forrest, T. Pham, S. Ma, B. Space, L. Wojtas, M. Eddaoudi, M. J. Zaworotko, *Nature* **2013**, *495*, 80–84; e) P. D. C. Dietzel, B. Panella, M. Hirscher, R. Blom, H. Fjellvåg, *Chem. Commun.* **2006**, 959–961; f) P. D. C. Dietzel, R. E. Johnsen, R. Blom, H. Fjellvåg, *Chem. Eur. J.* **2008**, *14*, 2389–2397.
- [22] S. Bruker-AXS, version 2013.8, **2013**, Bruker-AXS, Madison, WI 53711, USA.
- [23] S. Bruker-AXS, version 2012.1, **2012**, Bruker-AXS, Madison, WI 53711, USA.
- [24] G. Sheldrick, *Acta Crystallogr. Sect. A* **2015**, *71*, 3–8.
- [25] G. Sheldrick, *Acta Crystallogr. Sect. C* **2015**, *71*, 3–8.
- [26] E. J. Gabe, Y. Le Page, J.-P. Charland, F. L. Lee, P. S. White, *J. Appl. Crystallogr.* **1989**, *22*, 384–387.
- [27] S. J. Clark, M. D. Segall, C. J. Pickard, P. J. Hasnip, M. J. Probert, K. Refson, M. C. Payne, *Kristallogr.* **2005**, *220*, 567–570.
- [28] J. P. Perdew, K. Burke, M. Ernzerhof, *Phys. Rev. Lett.* **1996**, *77*, 3865–3868.
- [29] S. Grimme, *J. Comput. Chem.* **2006**, *27*, 1787–1799.
- [30] a) C. J. Pickard, F. Mauri, *Phys. Rev. B* **2001**, *63*, 245101; b) J. R. Yates, C. J. Pickard, F. Mauri, *Phys. Rev. B* **2007**, *76*, 024401.
- [31] H. E. Gottlieb, V. Kotlyar, A. Nudelman, *J. Org. Chem.* **1997**, *62*, 7512–7515.
- [32] C. Dybowski, G. Neue, *Prog. Nucl. Magn. Reson. Spectrosc.* **2002**, *41*, 153–170.
- [33] K. Eichele, *Wsoleds1*, University of Tübingen, Tübingen (Germany), **2009**.
- [34] a) J. Hu, T. Sun, X. Ren, S. Wang, *Microporous Mesoporous Mater.* **2015**, *204*, 73–80; b) I. Spanopoulos, I. Bratsos, C. Tampaxis, A. Kourtellis, A. Tasiopoulos, G. Charalambopoulou, T. A. Steriottis, P. N. Trikalitis, *CrytEngComm* **2015**, *17*, 532–539.
- [35] M. Fischer, *Microporous Mesoporous Mater.* **2016**, *219*, 249–257.
- [36] L. C. Snyder, *J. Chem. Phys.* **1978**, *68*, 291–294.
- [37] M. J. Duer, in *NMR Techniques for Studying Molecular Motion in Solids*, Blackwell Science, New York, **2002**.
- [38] a) R. Poupkov, Z. Luz, A. J. Vega, H. Zimmermann, *J. Chem. Phys.* **1987**, *86*, 5358–5364; b) A. Hauch, H. Bildsøe, H. J. Jakobsen, J. Skibsted, J.

- Magn. Reson.* **2003**, *165*, 282–292; c) S. Antonijevic, S. Wimperis, *J. Chem. Phys.* **2005**, *122*, 044312.
- [39] a) S. K. Vasa, H. Janssen, E. R. H. Van Eck, A. P. M. Kentgens, *Phys. Chem. Chem. Phys.* **2011**, *13*, 104–106; b) T. Kobayashi, K. Mao, P. Paluch, A. Nowak-Król, J. Sniechowska, Y. Nishiyama, D. T. Gryko, M. J. Potrzebowski, M. Pruski, *Angew. Chem. Int. Ed.* **2013**, *52*, 14108–14111; *Angew. Chem.* **2013**, *125*, 14358–14361; c) M. P. Hanrahan, A. Venkatesh, S. L. Carnahan, J. L. Calahan, J. W. Lubach, J. Munson, A. J. Rossini, *Phys. Chem. Chem. Phys.* **2017**, *19*, 28153–28162.
- [40] G. Mali, J. Trebosc, C. Martineau, M. Mazaj, *J. Phys. Chem. C* **2015**, *119*, 7831–7841.
- [41] J. Xu, V. V. Terskikh, Y. Chu, A. Zheng, Y. Huang, *Chem. Mater.* **2015**, *27*, 3306–3316.
- [42] a) Z. Chen, C. S. Wannere, C. Corminboeuf, R. Puchta, P. V. R. Schleyer, *Chem. Rev.* **2005**, *105*, 3842–3888; b) D. Sebastiani, *ChemPhysChem* **2006**, *7*, 164–175; c) A. Stanger, *J. Org. Chem.* **2006**, *71*, 883–893.
- [43] a) A. C. Forse, J. M. Griffin, V. Presser, Y. Gogotsi, C. P. Grey, *J. Phys. Chem. C* **2014**, *118*, 7508–7514; b) K. Li, Z. Bo, J. Yan, K. Cen, *Sci. Rep.* **2016**, *6*, 39689.
- [44] S. K. Elsaidi, M. H. Mohamed, H. T. Schaefer, A. Kumar, M. Lusi, T. Pham, K. A. Forrest, B. Space, W. Q. Xu, G. J. Halder, J. Liu, M. J. Zaworotko, P. K. Thallapally, *Chem. Commun.* **2015**, *51*, 15530–15533.
- [45] K. Uemura, A. Maeda, T. K. Maji, P. Kanoo, H. Kita, *Eur. J. Inorg. Chem.* **2009**, 2329–2337.
- [46] a) C. E. Wilmer, M. Leaf, C. Y. Lee, O. K. Farha, B. G. Hauser, J. T. Hupp, R. Q. Snurr, *Nat. Chem.* **2012**, *4*, 83–89; b) A. Schoedel, Z. Ji, O. M. Yaghi, *Nat. Energy* **2016**, *1*, 16034.
- [47] N. L. Rosi, J. Kim, M. Eddaoudi, B. Chen, M. O’Keeffe, O. M. Yaghi, *J. Am. Chem. Soc.* **2005**, *127*, 1504–1518.
- [48] R. Mercado, B. Vlaisavljevich, L.-C. Lin, K. Lee, Y. Lee, J. A. Mason, D. J. Xiao, M. I. Gonzalez, M. T. Kapelewski, J. B. Neaton, B. Smit, *J. Phys. Chem. C* **2016**, *120*, 12590–12604.
- [49] X.-J. Hou, P. He, H. Li, X. Wang, *J. Phys. Chem. C* **2013**, *117*, 2824–2834.
- [50] P. Canepa, Y. J. Chabal, T. Thonhauser, *Phys. Rev. B* **2013**, *87*, 094407.

Manuscript received: January 27, 2018

Revised manuscript received: March 17, 2018

Accepted manuscript online: March 25, 2018

Version of record online: May 14, 2018